

Investigating Magnetostructural Correlations in the Pseudooctahedral $trans$ -[Ni^{II}{(OPPh₂)(EPh₂)N}₂(sol)₂] Complexes (E = S, Se; sol = DMF, THF) by Magnetometry, HFEPR, and ab Initio Quantum Chemistry

Dimitrios Maganas,^{†,‡} J. Krzystek,^{*,§} Eleftherios Ferentinos,[†] Alexander M. Whyte,[⊥] Neil Robertson,[⊥] Vassilis Psycharis,^{||} Aris Terzis,^{||} Frank Neese,^{*,‡} and Panayotis Kyritsis^{*,†}

[†]Inorganic Chemistry Laboratory, Department of Chemistry, National and Kapodistrian University of Athens, 15771 Athens, Greece

[§]National High Magnetic Field Laboratory, Florida State University, Tallahassee, Florida 32310, United States

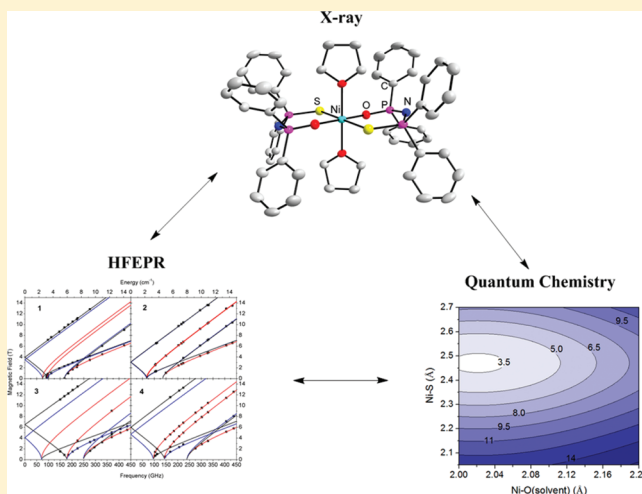
[⊥]School of Chemistry and EaStChem, University of Edinburgh, West Mains Road, Edinburgh EH9 3JJ, United Kingdom

^{||}Institute of Materials Science, NCSR "Demokritos", 15310 Aghia Paraskevi Attikis, Athens, Greece

[‡]Max-Planck Institute for Bioinorganic Chemistry, Mülheim an der Ruhr D-45470, Germany

Supporting Information

ABSTRACT: In this work, magnetometry and high-frequency and -field electron paramagnetic resonance spectroscopy (HFEPR) have been employed in order to determine the spin Hamiltonian (SH) parameters of the non-Kramers, $S = 1$, pseudooctahedral $trans$ -[Ni^{II}{(OPPh₂)(EPh₂)N}₂(sol)₂] (E = S, Se; sol = DMF, THF) complexes. X-ray crystallographic studies on these compounds revealed a highly anisotropic NiO₄E₂ coordination environment, as well as subtle structural differences, owing to the nature of the Ni^{II}-coordinated solvent molecule or ligand E atoms. The effects of these structural characteristics on the magnetic properties of the complexes were investigated. The accurately HFEPR-determined SH zero-field-splitting (zfs) D and E parameters, along with the structural data, provided the basis for a systematic density functional theory (DFT) and multiconfigurational ab initio computational analysis, aimed at further elucidating the electronic structure of the complexes. DFT methods yielded only qualitatively useful data. However, already entry level ab initio methods yielded good results for the investigated magnetic properties, provided that the property calculations are taken beyond a second-order treatment of the spin-orbit coupling (SOC) interaction. This was achieved by quasi-degenerate perturbation theory, in conjunction with state-averaged complete active space self-consistent-field calculations. The accuracy in the calculated D parameters improves upon recovering dynamic correlation with multiconfigurational ab initio methods, such as the second-order N -electron valence perturbation theory NEVPT2, the difference dedicated configuration interaction, and the spectroscopy-oriented configuration interaction. The calculations showed that the magnitude of D (~ 3 – 7 cm⁻¹) in these complexes is mainly dominated by multiple SOC contributions, the origin of which was analyzed in detail. In addition, the observed largely rhombic regime ($E/D = 0.16$ – 0.33) is attributed to the highly distorted metal coordination sphere. Of special importance is the insight by this work on the zfs effects of Se coordination to Ni^{II}. Overall, a combined experimental and theoretical methodology is provided, as a means to probe the electronic structure of octahedral Ni^{II} complexes.



INTRODUCTION

In the course of the past few years, investigations on the biological properties of nickel have been greatly advanced, affording vital structural and biochemical information.¹ The well-established structural and redox versatility of nickel in forming simple coordination compounds² is also manifested in its biochemical activity. In that respect, variable oxidation states of nickel, as well as a multitude of coordination geometries,

have been identified in the active site of Ni-containing enzymes.³ Extensive studies on biomimetic Ni^{II} complexes,⁴ as structural and functional analogues of metalloenzymes, such as the Ni-Fe hydrogenase^{5–7} or the CO dehydrogenase/acetyl

Received: February 29, 2012

Published: June 14, 2012

coenzyme A synthase,^{8,9} have been performed in the past and are continuously being pursued.

The square-planar (SP) Ni^{II} complexes are diamagnetic, although some rare and interesting exceptions have been identified experimentally and probed theoretically.^{10,11} On the other hand, octahedral Ni^{II} complexes are generally paramagnetic.² Toward the aim of fully describing the electronic structure of a paramagnetic metal site in either a metalloprotein or a simple transition-metal complex, the reliable determination of the *g* tensor components, along with the zero-field-splitting (zfs) parameters *D* (axial) and *E* (rhombic), is of paramount importance.¹² Specific physicochemical methods have been employed for the determination of the *g* and *D* tensors in paramagnetic systems,¹³ among which magnetometry has been frequently employed as the only method for mononuclear Ni^{II} complexes.^{14–16} However, in the absence of corroborative data from other physicochemical methods, the reliability of the results derived can be questioned, especially for highly rhombic systems (vide infra). Moreover, *S* = 1 Ni^{II} systems, of either tetrahedral (*T_d*) or octahedral (*O_h*) geometry, are usually not amenable to conventional X-band electron paramagnetic resonance (EPR) studies because of their large *D* values.¹² However, high-frequency and -field EPR spectroscopy (HFEP) has been successfully applied for the investigation of Ni^{II} complexes of various coordination spheres and geometries.^{17–29} It should be stressed that magnetic circular dichroism (MCD) studies,³⁰ as well as empirical ligand-field theory (LFT) analysis based on data by Ni L-edge X-ray absorption spectroscopy,³¹ have provided evidence of large *D* values (44–76 cm⁻¹) for both inorganic and bioinorganic Ni^{II} sites of *T_d* geometry, which would render them “EPR-silent”, even at the highest frequencies and fields currently available. More recently, frequency domain magnetic resonance spectroscopy (FDMRS) was also employed for the direct determination of *D* in mononuclear Ni^{II} complexes.^{23,27,32,33}

Various experimental investigations on the magnetic properties of *O_h* *S* = 1 Ni^{II} systems have been recently reviewed.^{12,34} Of particular importance are combined studies, by magnetometry, HFEP, and FDMRS, on *O_h* Ni^{II} complexes exhibiting NiN₄O₂,^{23,29a} NiN₃O₃,²⁶ and NiN₂O₄²⁴ coordination spheres, which afforded accurate *g* and zfs parameters. However, these studies have been carried out on systems of disparate coordination spheres, and therefore it has not yet been possible to systematically discern magnetostuctural correlations in this class of Ni^{II} systems.

Hence, in this work, a series of pseudooctahedral complexes, namely, *trans*-[Ni{(OPPh₂)(EPPPh₂)N₂(sol)₂}]₂ [E = S, Se; sol = *N,N*-dimethylformamide (DMF),³⁵ tetrahydrofuran (THF); Scheme 1], were studied by magnetometry, HFEP, and computational methods. These complexes contain a NiO₄E₂ coordination sphere, which has not yet been investigated by any

of the above methods.¹² In addition, these systems exhibit subtle and well-defined structural differences, owing to the nature of the Ni^{II}-coordinated solvents (DMF or THF) and E ligand atoms (S or Se), thus making it possible to investigate structural effects on their magnetic behavior.

Furthermore, in this work, advanced quantum-chemical calculations were performed, aiming at further elucidating the electronic structure of these open-shell, *S* = 1, systems, in the framework of the spin Hamiltonian (SH) formalism.^{36,37} Thus, the experimentally determined zfs parameters were translated into electronic structure elements, by applying density functional theory (DFT) and multireference-correlated ab initio methods. Collectively, the experimental and theoretical investigations described herein helped to explain the observed magnetic anisotropy in this class of Ni^{II} complexes, by probing the effects on the *g* and zfs parameters of subtle structural changes in their coordination sphere.

MATERIALS AND METHODS

Synthesis. The synthesis of *trans*-[Ni{(OPPh₂)(EPPPh₂)N₂(DMF)₂}]₂ [E = S (1), Se (2)] was accomplished by employing the recently described literature method.³⁵ The synthesis of *trans*-[Ni{(OPPh₂)(EPPPh₂)N₂(THF)₂}]₂ [E = S (3), Se (4)] is described in the Supporting Information (SI).

IR Spectroscopy. IR spectra were run in the range 4000–200 cm⁻¹ on a Perkin-Elmer 883 IR spectrophotometer, as KBr disks.

X-ray Crystal Structure Determination. A colorless crystal of 3 (0.10 × 0.32 × 0.44 mm³) and a yellow crystal of 4 (0.18 × 0.39 × 0.48 mm³) were taken from the mother liquor and immediately cooled to –113 °C. Diffraction measurements were made on a Rigaku R-Axis SPIDER image plate diffractometer using graphite-monochromated Cu Kα radiation. Further experimental details are presented in the SI.

Magnetometry. Magnetic susceptibility measurements were performed on powder samples of 3 and 4 from 1.8 to 300 K using a Quantum Design MPMS-XL SQUID magnetometer with MPMS MultiVu Application software to process the data. The magnetic field used was 0.1 T. Diamagnetic corrections were applied to the observed paramagnetic susceptibilities by using Pascal's constants.³⁸

HFEP Spectroscopy. HFEP spectra of 1–4 were recorded using a spectrometer based on a 15/17 T superconducting magnet, differing from that already described³⁹ only by the use of a Virginia Diodes Inc. source operating at a base frequency of 12–14 GHz and increased by a cascade of multipliers.

Analysis of Magnetometry and HFEP Data. The variable-temperature magnetic susceptibility and the multifrequency HFEP data were fitted using the same SH of an *S* = 1 system, comprised of Zeeman (*g* tensor) and second-rank zfs *D* and *E* components (eq 1):

$$\hat{H}_{spin} = \beta_e \hat{B} \cdot \mathbf{g} \cdot \hat{S} + D[S_z^2 - S(S+1)/3] + E(S_x^2 - S_y^2) \quad (1)$$

in which β_e is the electron Bohr magneton. A full analytical solution of the SH eigenvalue problem for the *S* = 1 case can be found in textbooks.^{40,41}

The magnetometry data were fitted to the susceptibility expression for an isolated *O_h* Ni^{II} complex, with an additional χ_{TIP} term in order to account for any unaccounted diamagnetic contributions, as well as the temperature-independent component from the metal ion.⁴²

Field-swept HFEP spectra on polycrystalline solids provided turning points in powder-pattern spectra. Their frequency dependencies were recorded as two-dimensional maps of resonances, as a function of the excitation frequency (or energy) along the principles of tunable-frequency EPR.⁴³ The SH parameters were then fitted to these data by use of a nonlinear least-squares procedure, based on the well-known formulas resulting from the exact solution of the equations for the triplet states of arbitrary orientation.⁴⁴

Theory. The zfs, expressed in terms of the *D* tensor, is the leading SH parameter for systems with a spin ground state *S* > 1/2.¹⁴ The zfs describes the lifting of the degeneracy of the 2*S* + 1 magnetic sublevels

Scheme 1. Complexes Studied in This Work

<i>trans</i> -[Ni{(OPPh ₂)(EPPPh ₂)N ₂ (sol) ₂ }] ₂	<i>sol</i>	
	<i>dmf</i>	<i>thf</i>
<i>E</i>		
<i>S</i>	1	3
<i>Se</i>	2	4

$M_s = S, S - 1, \dots, -S$, which are exactly degenerate at the level of the Born–Oppenheimer (BO) Hamiltonian, in the absence of an external magnetic field. To first order in the perturbation theory (PT), the zfs arises from the direct magnetic-dipole spin–spin interaction between unpaired electrons (spin–spin coupling, SSC). To second order, contributions arise from the spin–orbit coupling (SOC) of electronically excited states into the ground state. These effects can be phenomenologically collected in the usual SH expression:

$$\hat{H}_{zfs} = \hat{S} \cdot \mathbf{D} \cdot \hat{S} \quad (2)$$

where \hat{S} is the fictitious spin of the ground state. In a coordinate system that diagonalizes the \mathbf{D} tensor, eq 2 can be rewritten, as shown in eq 3, in which D and E represent the axial and rhombic components of the zfs, respectively.

$$\hat{H}_{zfs} = D[S_z^2 - S(S + 1)/3] + E(S_x^2 - S_y^2) \quad (3)$$

The choice of the axes is based on the $0 \leq E/D \leq 1/3$ convention. In the generalized $S = 1$ case, the zfs term in eq 3 gives rise to three magnetic sublevels, expressed by eq 4:

$$\begin{aligned} |+\rangle &= \cos \theta |1, +1\rangle + \sin \theta |1, -1\rangle \\ |0\rangle &= |1, 0\rangle \\ |-\rangle &= \sin \theta |1, +1\rangle - \cos \theta |1, -1\rangle \end{aligned} \quad (4)$$

where the angle θ , in terms of the zfs parameters, is given by

$$\tan(2\theta) = \sqrt{3} \frac{E}{D} \quad (5)$$

Although the spin states are characterized by $m_s = 0, \pm 1$, only at high magnetic fields, or when the field is parallel to the molecular axis, is it usual to denote the magnetic $|0\rangle, |+\rangle$, and $|-\rangle$ sublevels as $|0\rangle, |1, +1\rangle$, and $|1, -1\rangle$, respectively. In principle, because of the $\Delta m_s = \pm 1$ selection rule, two allowed EPR transitions are expected, namely, $|0\rangle \rightarrow |1, +1\rangle$ and $|0\rangle \rightarrow |1, -1\rangle$, the energy of which is equal to $|D| \pm |E|$, respectively. The SSC contributes to the zfs in first order of the PT and, therefore, can be calculated as an expectation value. The SOC contribution, however, arises in second order and, hence, is related to a complete sum over states that contain contributions from excited states of spin multiplicities different from the ground state.

Quasi-Degenerate PT (QDPT). In QDPT, one starts by obtaining an approximate solution of the BO Hamiltonian of a multireference type, such as the complete-active-space self-consistent-field (CASSCF) multireference configuration interaction (MRCI), which yields a many particle wave function in the form of $|\Psi_I^{SS}\rangle = \sum_{\mu} C_{\mu I} |\Phi_{\mu}^{SS}\rangle$. Here, the upper indices SS stand for a many-particle wave function with spin quantum number S and spin projection quantum number $M_S = S$. Because the BO Hamiltonian does not contain any complex-valued operator, the $|\Psi_I^{SS}\rangle$ solutions may be chosen to be real-valued. The introduction of SOC requires the lift over of the $2S + 1$ degeneracy of the total spin S \hat{H}_{BO} eigenfunctions. Thus, the basis of the treatment is the $|\Psi_I^{SM}\rangle$ states, in which I covers all of the roots calculated in the first step of the procedure and $M = -S, \dots, S$ enumerates all members of a given multiplet. Matrix elements over the $|\Psi_I^{SM}\rangle$ functions are readily generated using the Wigner–Eckart theorem because all $2S + 1$ members of the multiplet share the same spatial part of the wave function.⁴⁵

On the basis of the above functions, SOC and SSC effects, along with the Zeeman interaction, can be taken into account by means of QDPT, which amounts to diagonalization of the matrix representation of $\hat{H}_{BO} + \hat{H}_{SOC} + \hat{H}_{SSC} + \hat{H}_Z$ on the basis of the $|\Psi_I^{SM}\rangle$ states:

$$\begin{aligned} \langle \Psi_I^{SM} | \hat{H}_{BO} + \hat{H}_{SOC} + \hat{H}_{SSC} + \hat{H}_Z | \Psi_J^{S'M'} \rangle \\ = \delta_{IJ} \delta_{SS} \delta_{MM} E_I^{(S)} + \langle \Psi_I^{SM} | \hat{H}_{SOC} + \hat{H}_{SSC} + \hat{H}_Z | \Psi_J^{S'M'} \rangle \end{aligned} \quad (6)$$

Diagonalization of this matrix yields the energy levels and eigenvectors of the coupled states $\{\Psi_I^{SM}\}$. This procedure yields the \mathbf{g} and \mathbf{D} tensors directly. Alternatively, the SOC components of \mathbf{D} are calculated through well-established second-order PT equations:⁴⁶

$$D_{kl}^{\text{SOC}-(0)} = -\frac{1}{S^2} \sum_{b(S_b=S)} \Delta_b^{-1} \langle 0SS | \sum_i z_{k;i}^{\text{SOMF}} \hat{s}_{i;z} | bSS \rangle \langle bSS | \sum_i z_{l;i}^{\text{SOMF}} \hat{s}_{i;z} | 0SS \rangle \quad (7)$$

$$D_{kl}^{\text{SOC}-(1)} = -\frac{1}{2S(S-1)} \sum_{b(S_b=S-1)} \Delta_b^{-1} \langle 0SS | \sum_i z_{k;i}^{\text{SOMF}} \hat{s}_{i;+1} | b(S-1)(S-1) \rangle \langle b(S-1)(S-1) | \sum_i z_{l;i}^{\text{SOMF}} \hat{s}_{i;-1} | 0SS \rangle \quad (8)$$

$$D_{kl}^{\text{SOC}-(+1)} = -\frac{1}{(S+1)(2S+1)} \sum_{b(S_b=S+1)} \Delta_b^{-1} \langle 0SS | \sum_i z_{k;i}^{\text{SOMF}} \hat{s}_{i;-1} | b(S+1)(S+1) \rangle \langle b(S+1)(S+1) | \sum_i z_{l;i}^{\text{SOMF}} \hat{s}_{i;+1} | 0SS \rangle \quad (9)$$

The first term (eq 7) describes contributions from excited states of the same spin as that of the ground state ($S' = S$), whereas the second and third terms (eqs 8 and 9) arise from states with $S' = S - 1$ and $S' = S + 1$, respectively. Here, k and l denote Cartesian components x, y , and z , and Δ_b is the energy difference between the ground state and the b th excited state, in the absence of SOC interaction. Here and throughout the paper, the SOC interaction has been quantified by the spin–orbit mean-field (SOMF) method, in the implementation already described.⁴⁷ In this approach, the SOC appears as an effective one-electron operator of the form $\hat{H}_{\text{SOMF}} = \sum_i z_{i;\alpha}^{\text{SOMF}} \hat{s}_{i;\alpha}$.

Computational Details. All calculations were performed using the ORCA computational package.⁴⁸ For the DFT calculations, the crystallographic structures of **1**,³⁵ **2**,³⁵ **3**, and **4** were employed, using the BP86 and B3LYP^{49–51} functionals for geometries/frequencies and spectroscopic properties, respectively. Ahlrich's polarized triple- ζ (TZVP)-quality⁵² basis set was employed for all atoms, in combination with the TZV/J Coulomb fitting basis for the resolution of identity (RI) approximation (in BP86 calculations). For geometry optimizations, a one-center relativistic correction was applied, by employing the implemented standard second-order Douglas–Kroll–Hess procedure.^{53–55}

To make the ab initio calculations feasible and to allow for direct comparisons with DFT studies, a second set of calculations was performed in which the bulky Ph groups of the studied complexes were replaced by H atoms. This leads to the corresponding model complexes, denoted as **H1**, **H2**, **H3**, and **H4**, the structural coordinates of which correspond to fully optimized structures by the DFT methods described above. Alternatively, these coordinates were taken from the crystallographic structures, and only the H positions were optimized. In addition, the $[\text{Ni}\{\text{(OPH}_2\text{)}\text{(OPH}_2\text{)N}\}_2(\text{DMF})_2]$ model **H5** was constructed from the crystallographic structure of $[\text{Ni}\{\text{(OPPh}_2\text{)}\text{(OPPh}_2\text{)N}\}_2(\text{DMF})_2]$ (**5**),⁵⁶ in which both the Ph peripheral groups of the ligands and the Me groups of the DMF molecule were replaced by H atoms. This structure preserves high symmetry (D_{2h}) around the Ni^{II} center, and, thus, it will serve as a reference structure for our calculations. The zfs DFT calculations were performed by employing the generalized gradient approximation (GGA) BP86, the hybrid-GGA B3LYP, the meta-GGA TPSS,⁵⁷ and the TPSSH⁵⁸ density functionals, together with the def2-TZVP(-f)⁵⁹ basis set. Both the coupled-perturbed method (CP-SOC)⁶⁰ in its original form and in the variant recently proposed by van Wüllen,⁶¹ and the Pederson–Khanna⁶² approach were used for calculation of the D^{SOC} part of the zfs. In addition, the D^{SS} part that accounts for the SSC contribution to the zfs is treated with the unrestricted natural orbital (UNO) option. This allows for calculation of the SSC term, with a restricted spin density obtained from the singly occupied UNOs. The objective of this procedure is discussed elsewhere.^{63,64} In ab initio calculations, for all atoms the higher-accuracy basis set def2-TZVP(-f)⁵⁹ was used,

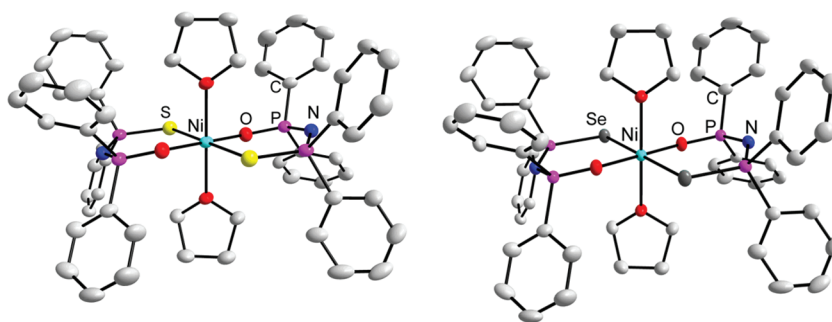


Figure 1. X-ray crystal structures of *trans*-[Ni{(OPPh₂)(EPPH₂)N₂}(THF)₂] [E = S (3, left), Se (4, right)] with thermal ellipsoids shown at 30%. The H atoms are omitted for clarity. Atom color coding: Ni, cyan; O, red; S, yellow; Se, dark gray; P, magenta; N, blue; C, light gray.

Table 1. SH Parameters for the Investigated Complexes (#), Obtained from Magnetic Susceptibility Data (Susc), as Well as from Best Fits to the Two-Dimensional Maps of HFEPRs

#	D (cm ⁻¹) (Susc.)	D (cm ⁻¹) (HFEPR)	E (cm ⁻¹) (HFEPR)	E/D (HFEPR)	g _{iso} (Susc.)	g _x (HFEPR)	g _y (HFEPR)	g _z (HFEPR)
1	2.5 ^a	4.37(1)	1.23(1)	0.28	2.34 ^a	2.27(2)	2.27 ^b	2.259(6)
2		3.41(1)	1.11(1)	0.33	2.37 ^a	2.230(3)	2.235(3)	2.23 ^b
3	4.11(6)	7.11(1)	1.17(2)	0.16	2.302(3)	2.300(6)	2.293(7)	2.306(3)
4	4.85(4)	6.38(2)	1.59(2)	0.25	2.288(2)	2.269(4)	2.289(13)	2.203(7)

^aData from Ferentinos et al. *Dalton Trans.* 2011, 40, 169. ^bSet, not fitted.

together with the corresponding Coulomb fitting basis set. The minimal active space for ab initio calculations should include the five 3d-based molecular orbitals (MOs), involved in nonbonding or σ^* Ni–O/S/Se antibonding interactions, as well as the corresponding σ Ni–O/S/Se bonding MOs. This leads to an active space with 12 electrons in 7 orbitals [CAS(12,7)]. We have included all 10 roots for the $2S + 1 = 3$ (triplet) states arising from the ³F and ³P spectroscopic terms of Ni²⁺ and 15 roots for the $2S + 1 = 1$ (singlet) states arising from the corresponding ¹D, ¹G, and ¹S terms. Second-order N-electron valence perturbation theory (NEVPT2),^{65–67} the MR-difference-dedicated configuration interaction with 2 degrees of freedom (DDCI2), and the spectroscopy-oriented configuration interaction (SORCI)⁶⁸ calculations were performed on top of the state-averaged CASSCF reference wave functions, in order to recover the differential dynamic correlation between the ground and excited states. As explained previously,⁶⁹ we have used individual selection in the SORCI calculations, in order to decrease the computational burden. The relevant thresholds are $T_{\text{sel}} = 10^{-6}$ Eh and $T_{\text{pre}} = 10^{-5}$.

RESULTS AND DISCUSSION

Synthesis. The synthesis and characterization of complexes 1 and 2 has already been described.³⁵ Complexes 3 and 4 were isolated upon crystallization of [Ni{(OPPh₂)(EPPH₂)N₂}] (E = S or Se) by a THF/*n*-hexane solvent system. More information, including elemental analysis and IR data, are presented in the SI.

X-ray Crystallography. The X-ray crystallographic structures of 1 and 2 have been reported previously,³⁵ whereas those of 3 and 4 are presented herein. The crystal data and refinement characteristics are shown in Table S1 in the SI. The ORTEP representations of the crystal structures of 3 and 4 are shown in Figure 1, and selected bond lengths and angles are listed in Table S2 in the SI. Collectively, the structures of 1–4 correspond to the generic formula *trans*-[Ni{(OPPh₂)(EPPH₂)N₂}(sol)₂] (E = S, Se; sol = DMF, THF). All structures contain a center of symmetry, with discrete monomeric molecules exhibiting distorted octahedral NiO₄E₂ cores, in which Ni^{II} is coordinated by two equatorial (O, E) chelates in a *trans* arrangement as expected by symmetry, whereas the two axial

coordination sites are taken by the O atom of two solvent molecules.

For 3, the equatorial Ni–O and N–S bond lengths are 2.014(2) and 2.5343(7) Å, whereas for 4, the corresponding Ni–O and N–Se bond lengths are 2.001(2) and 2.5769(3) Å, respectively. For both complexes, the large difference between the two equatorial bond lengths reflects a significant deviation from the ideal *O_h* geometry. The Ni–Se bond length in 4 is 0.043 Å larger compared with the Ni–S bond length in 3. The corresponding difference between complexes 2 and 1 is significantly larger (0.115 Å).³⁵

On the other hand, the two axial Ni–O(THF) bond lengths, for 3 and 4, are 2.151(2) and 2.140(2) Å, respectively, which are slightly larger compared with the corresponding Ni–O(DMF) bond length in 1 [2.068(1) Å] and 2 [2.074(2) Å],³⁵ as well as with the analogous [Ni{(OPPh₂)(OPPh₂)N₂}(DMF)₂] complex [2.0922(18) Å].⁵⁶ On the basis of that above, the difference in the Ni–O(sol) bond length between complexes 1 and 3 and complexes 2 and 4 amounts to 0.082 and 0.066 Å, respectively.

As was also observed for 1 and 2,³⁵ the Ni–O_{eq} bond lengths for 3 and 4 are larger by only 0.067 and 0.060 Å, respectively, compared with those in the corresponding *T_d* [Ni{(OPPh₂)(EPPH₂)N₂}] complexes (E = S, average 1.947 Å;⁷⁰ E = Se, average 1.941 Å³⁵). On the other hand, the corresponding Ni–E bond lengths of 3 and 4 are larger by 0.239 and 0.162 Å, respectively, compared with those in [Ni{(OPPh₂)(EPPH₂)N₂}] (E = S, average 2.295 Å;⁷⁰ E = Se, average 2.414 Å³⁵). The above differences reveal a remarkable weakening of the Ni–E bonds in pseudooctahedral 3 and 4 compared with the corresponding *T_d* [Ni{(OPPh₂)(EPPH₂)N₂}] complexes.

Magnetic Properties. The magnetic susceptibility data for 3 and 4 were analyzed by the procedure already described for 1 and 2.³⁵ As was shown for the latter, 3 and 4 exhibit qualitatively the same behavior at low temperature, showing a sharp drop of χT (at $T < 15$ K from maximal values of $\mu_{\text{eff}} = 3.24$ – 3.32). This range is within that expected for the spin-only value for a spin triplet ($\mu_{\text{eff}} = 2.83$; $g = 2.00$) with some additional second-order orbital contribution. The low-temper-

ature drop in χT is a direct consequence of zfs .^{14,71} The magnitude of the axial D zfs component was estimated by fitting the susceptibility data for each complex (Table 1).⁴² Both **3** and **4** showed Curie–Weiss behavior above around 15 K, with a negligible Weiss constant, as would be expected for metal centers largely isolated by the bulky ligand shell. For complex **3**, the Curie constant C was determined to be $1.35 \text{ cm}^3 \text{ K mol}^{-1}$ from the plot of χT against T (Figure 2), whereas for

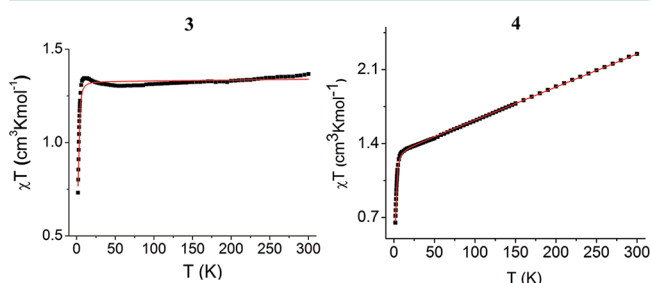


Figure 2. Plot of χT against T for **3** and **4** showing the constant value of $\chi T = \text{Curie constant} = 1.35 \text{ cm}^3 \text{ K mol}^{-1}$ between 300 and 15 K for **3** and an estimated value of the Curie constant = $1.38 \text{ cm}^3 \text{ K mol}^{-1}$ for **4**, partly obscured by the continuing gradual rise with T . The abrupt drop at low temperature is attributed to zfs , and the red continuous line shows a simulation with $g = 2.302(3)$ and $|D| = 4.11 \text{ cm}^{-1}$ (for **3**) and $g = 2.288(2)$ and $|D| = 4.85 \text{ cm}^{-1}$ (for **4**).

complex **4**, as was also the case with **2**,³⁵ the Curie constant could only be approximated as $1.38 \text{ cm}^3 \text{ K mol}^{-1}$ because of the continuing gradual rise of the χT product observed at $T > 15 \text{ K}$. A similar behavior has been previously observed also for $V^{III} O_h$ complexes.⁷² In fact, the notable failure of χT to level off with T has been attributed to a number of factors accounting for the intermolecular interactions between the microcrystalline particles, as well as the inaccuracy in the estimation of the

diamagnetic component from Pascal's constants. Another possible source is the contribution of the excited electronic states, which give rise to some unaccounted temperature-independent components (TIP).^{14,71} Also, the observed behavior of **4** could be, in part, due to a temperature-independent component arising from a highly paramagnetic or ferromagnetic impurity.

In addition, the values of the Curie constant for complexes **3** and **4** lead to values of $g = 2.302$ (**3**) and 2.288 (**4**), respectively, toward the higher end of O_h Ni^{II} complexes in the literature, compared with typical values of around 2.25.^{73,74} Similar behavior was previously observed for complexes **1** and **2**,³⁵ with $g = 2.34$ and 2.37 , respectively (Table 1). In fact, for an ideal octahedron, the g value can be calculated using eq 10:

$$g = 2 \left(1 - \frac{2\zeta^{SOC}}{\Delta_{oct}} \right) \quad (10)$$

where ζ^{SOC} is the one-electron SOC constant and Δ_{oct} is the octahedral crystal-field-splitting parameter.⁷⁵ This describes the extent of mixing of the ground state with excited states through SOC and, hence, is proportional to ζ^{SOC} and inversely proportional to Δ_{oct} . By using the value of $\zeta^{SOC} = -668 \text{ cm}^{-1}$ for $Ni^{2+}(g)$,⁷⁶ we calculate an upper limit of $\Delta_{oct} \sim 8850 \text{ cm}^{-1}$ ($g = 2.302$) and 9280 cm^{-1} ($g = 2.288$) for complexes **3** and **4**, respectively, which are only moderately larger compared with the unusually small estimates of Δ_{oct} obtained for complexes **1** and **2**.³⁵ On the other hand, by using the g_x , g_y , and g_z values obtained by EPR for complex **4** (Table 1), the upper limit of Δ_{oct} is calculated to be between 9250 and 13160 cm^{-1} because g_z is rather smaller in this case. The deviation from ideal O_h behavior may be expected because of the lower symmetry of **1–4**; however, the estimated crystal-field splitting is relatively small compared with more typical values exceeding 10000 cm^{-1} .⁷⁷ The consistency in the observed behavior for **1–**

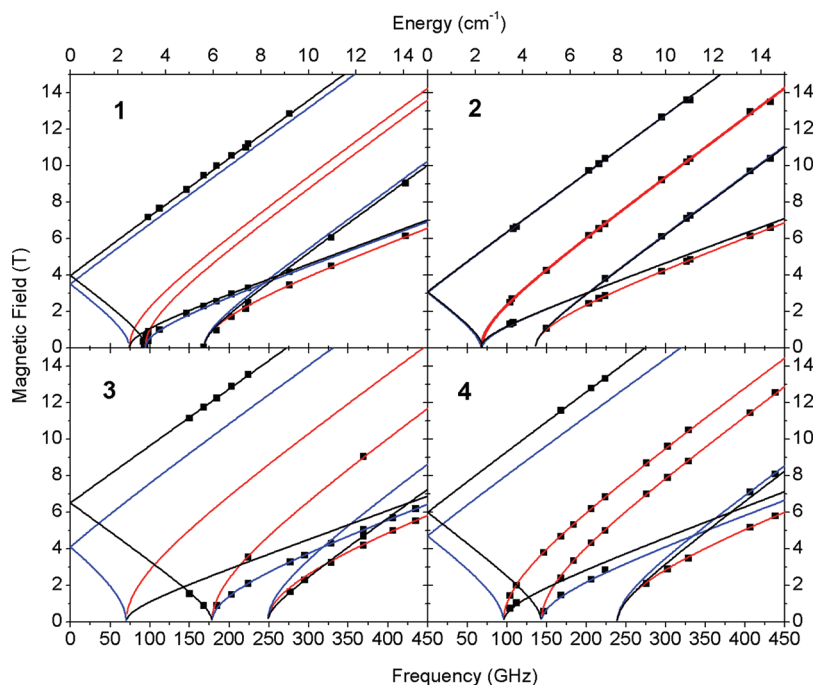


Figure 3. Two-dimensional field vs frequency (or quantum energy) maps of EPR turning points for complexes **1–4**. The squares represent experimental points, whereas the curves were simulated using best-fit SH parameters listed in Table 1. Red curves denote turning points with $B_0 \parallel x$, blue curves with $B_0 \parallel y$, and black curves with $B_0 \parallel z$. The data set was collected at $T = 10 \text{ K}$.

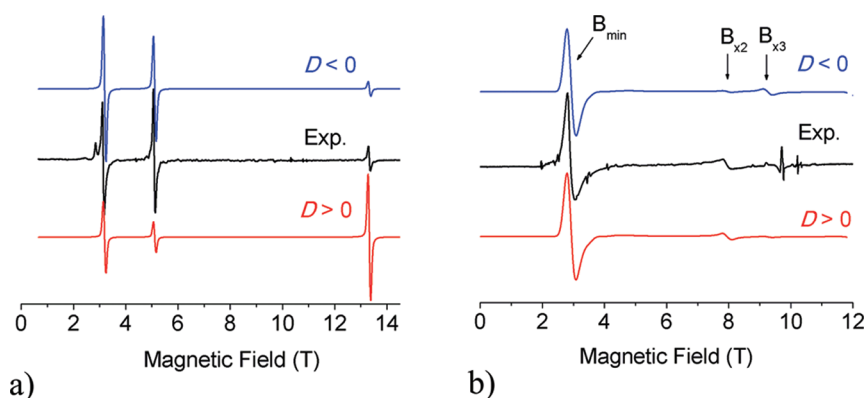


Figure 4. (a) EPR spectrum of complex **4** as an unrestrained powder at 302.4 GHz and 10 K (black trace), accompanied by simulations of a single-crystal spectrum, under the same conditions (colored traces). Simulation parameters: $|D| = 5.70 \text{ cm}^{-1}$, $|E| = 1.20 \text{ cm}^{-1}$, and $g_{\text{iso}} = 2.37$, crystal oriented with respect to the field by polar angles $(\theta, \varphi) = (21.5^\circ, 28^\circ)$. The blue trace represents a negative D and the red trace a positive value of that parameter. (b) EPR spectrum of complex **4** as a pellet pressed with *n*-eicosane at 302.4 GHz and 10 K (black trace) accompanied by powder-pattern simulations (colored traces). Simulation parameters: $|D| = 6.38 \text{ cm}^{-1}$, $|E| = 1.69 \text{ cm}^{-1}$, and $g = [2.30, 2.25, 2.20]$. Single-crystal line width isotropic 120 mT. The blue trace represents a negative D and the red trace a positive value of that parameter. Particular turning points identified in the spectrum are labeled according to the terminology of Wasserman et al.⁷⁸ The group of resonances at about 10 T appears only after grinding of the sample and is thus attributed to decomposition products.

4 is noticeable and points toward a common origin in the unusual characteristics of these complexes. In particular, we note the unusually large Ni–E (E = S, Se) bond lengths discussed above, which would lead to a much weakened crystal field compared with a more typical O_h complex. On the basis of that above, it could be stated that a simplistic LFT type of approach provides only a qualitative insight into the nature of the SH parameters, and care should be taken when it is employed for quantitative predictions. Indeed, qualitatively, the magnetometry data reveal significant magnetic anisotropy in complexes **1**–**4**. However, on the basis of these data, it is not possible to unambiguously determine the magnitude or the sign of D . This is mainly due to the fact that the implemented fitting procedure excludes the rhombic E zfs parameter because, in this case, the fit would be overparametrized and, consequently, would not lead to meaningful results. The estimated D values are listed in Table 1, for comparison with the more accurate data extracted by HF-EPR, as described in the next section.

HF-EPR. All investigated complexes showed distinct problems in achieving a perfect random distribution of crystallites with regard to the magnetic field and thus produced spectra that were far from perfect powder patterns. Reducing the size of crystallites by grinding was only moderately successful because of a propensity of the complexes to lose the solvent molecule and convert to “EPR-silent” T_d $\text{Ni}[(\text{OPPh}_2)(\text{EPPPh}_2)\text{N}]_2$ complexes (Krzystek, J.; Kyritsis, P. Unpublished observations) or decompose in some other way. In addition, grinding had a rather counterintuitive effect of increasing the field-induced torquing effects, which could not be completely overcome with the usual methods of constraining the crystallites by pressing them into pellets. In the end, only complex **4** was found to be “well-behaved” enough to produce spectra that were of single-crystal quality when the sample was allowed to torque, or of a powder quality when pressed into a pellet. We will briefly discuss each particular complex and their EPR characteristics below.

Complex **1** produced a very strong EPR response but very poor quality spectra (Figure S1 in the SI). It was possible, however, by carrying out multifrequency EPR measurements to collect enough turning points in the spectra, so as to be able to

perform a least-squares fit of the SH parameters, with the results shown in Table 1. Particularly helpful were the values of two zero-field resonances, corresponding to the $|D| - |E|$ and $|D| + |E|$ transitions (Figure 3). The obtained $|D|$ value of 4.37 cm^{-1} is in the range previously observed for O_h Ni^{II} complexes^{12,24,29a} and the zfs tensor is highly rhombic ($E/D = 0.28$). The sign of D could not be determined, but with such high rhombicity of the zfs tensor, this parameter loses its relevance. The g values are close to isotropic at 2.26–2.27.

Complex **2** was very similar in its characteristics to **1**. It showed a strong propensity to torque in field when ground. When constrained in a pellet, it did not produce a powder spectrum of high quality (Figure S2 in the SI). Still, it was possible to simulate that spectrum, to a certain degree, using a powder pattern and by the multifrequency EPR approach (Figure 3) to extract the relevant SH parameters listed in Table 1. The magnitude of $|D|$ (3.4 cm^{-1}) is similar to complex **1**; what is notable is the closeness to the maximum rhombicity of the zfs tensor, with E/D approaching $1/3$. The g -factor values are practically isotropic at 2.23–2.24.

Complex **3**, as an unrestrained sample, produced EPR spectra that were uninterpretable. When ground and pressed into a pellet, it showed spectra of excessive line width that were similarly uninformative. We thus collected spectra from a minimally ground and immobilized solid. Even if these spectra were far from an ideal powder pattern, we could recognize some turning points (Figure S3 in the SI) and collect enough information to perform a least-square fit of the SH parameters to the two-dimensional map, with the results shown in Table 1 and Figure 3. The zfs parameter $|D|$ is of much larger magnitude (7.11 cm^{-1}) than those of complexes **1** and **2**, and the zfs tensor is much less rhombic ($E/D = 0.16$) than that in those complexes.

Complex **4** initially produced spectra of similarly low quality as the other complexes. However, when unrestrained, upon repeated field sweeps, it underwent an almost complete alignment of the crystallites in the magnetic field, with the resulting spectra being reasonably well-simulated, assuming a single-crystal behavior (Figure 4a). The parameters used in the simulations suggested zfs on the same order of magnitude as

that in complex 3, with D about 5.7 cm^{-1} and negative. Upon pressing into a pellet, the same sample generated a well-defined powder pattern that could be very well-simulated using $|D| = 6.38\text{ cm}^{-1}$, $|E| = 1.69\text{ cm}^{-1}$, and somewhat anisotropic g values from 2.2 to 2.3 (Figure 4b). Importantly, the pellet simulation proved unequivocally that the sign of D is positive, and the result obtained from the field-aligned sample was an artifact, most probably due to a nonperfect alignment. The final set of SH parameters was obtained for complex 4 in the same way as that for the other complexes, i.e., by a least-squares fit to the two-dimensional map of resonances (Figure 3), and found to be very close to that used in the pellet simulation ($D = +6.38$; $E/D = 0.25$; anisotropic g matrix from 2.20 to 2.29).

Quantum-Chemical Calculations. Geometric Considerations. We have recently performed extensive quantum-chemical calculations on the families of T_d $[\text{Ni}\{(\text{SPR}_2)(\text{SPR}'_2)\text{N}\}_2]$ ⁷⁹ and $[\text{Ni}\{(\text{SPR}_2)(\text{OPR}'_2)\text{N}\}_2]$,³⁵ which contain $\text{Ni}^{\text{II}}\text{S}_4$ and $\text{Ni}^{\text{II}}\text{S}_2\text{O}_2$ coordination spheres, respectively. The former are stabilized along either (i) the spin-conserving $D_{2d} \rightarrow C_{2v(\text{I})}$ or (ii) the spin-flipping $D_{2d} \rightarrow D_2 \rightarrow C_i$ isomerization pathways.⁷⁹ A number of crystallographically characterized compounds can be respectively identified at various points of these interconversion pathways, like (i) the D_{2d} $[\text{Ni}\{(\text{SP}^i\text{Pr}_2)_2\text{N}\}_2]$ ⁸⁰ and $[\text{Ni}\{(\text{SPPH}_2)_2\text{N}\}_2]$ ^{81,82} complexes, as well as the $C_{2v(\text{I})}$ $[\text{Ni}\{(\text{SPMe}_2)_2\text{N}\}_2]$ ⁸³ complex, or (ii) the C_i $[\text{Ni}\{(\text{SPPH}_2)_2\text{N}\}_2]$,⁸⁴ $[\text{Ni}\{(\text{SPPH}_2)(\text{SPMe}_2)\text{N}\}_2]$,⁸¹ and $[\text{Ni}\{(\text{SPPH}_2)(\text{SP}^i\text{Pr}_2)\text{N}\}_2]$ ⁷⁹ complexes. On the other hand, for the T_d $[\text{Ni}\{(\text{SPR}_2)(\text{OPR}'_2)\text{N}\}_2]$ complexes containing an asymmetric coordination sphere, relevant experimental structures along the corresponding interconversion pathway are provided by the $C_{2v(\text{I})}$ $[\text{Ni}\{(\text{OPPh}_2)(\text{SPR}'_2)\text{N}\}_2]$ ($R' = \text{Me}, \text{Ph}$) complexes.⁷⁰ Furthermore, in the presence of a coordinating solvent, an alternative spin-conserving $C_{2v(\text{I})} \rightarrow C_{2v(\text{II})} \rightarrow O_h C_i$ pathway leads to the six-coordinate $O_h C_i$ complexes,³⁵ exemplified by the experimental structures of complexes 1–4. In addition, the $[\text{Ni}\{(\text{OPPh}_2)(\text{OPPh}_2)\text{N}\}_2(\text{DMF})_2]$ complex (5) reported by Cristurean et al.,⁵⁶ which is the only existing O_h Ni^{II} system bearing the symmetric $[(\text{OPPh}_2)(\text{OPPh}_2)\text{N}]^-$ ligand and Ni^{II} -coordinated solvent molecules, exhibits D_{2h} (i.e., elongated O_h) symmetry. In this case, the analogous T_d $[\text{Ni}\{(\text{OPPh}_2)(\text{OPPh}_2)\text{N}\}_2]$ complex does not seem to be stable because only the binuclear $[\text{Ni}_2\{(\text{OPPh}_2)_2\text{N}\}_4]$ complex has been synthesized and characterized.⁵⁶ A BP86/TZVP/TZVPP geometry optimization on the $[\text{Ni}\{(\text{OPH}_2)(\text{OPH}_2)\text{N}\}_2(\text{DMF})_2]$ model (H^5) leads to a $C_{2v(\text{I})}$ geometry. Therefore, in the presence of a coordinating solvent, this system is expected to be stabilized along the $C_{2v(\text{I})} \rightarrow C_{2v(\text{II})} \rightarrow O_h C_i$ interconversion pathway, in agreement with the experimental observations.⁵⁶ In the following, the highly symmetric D_{2h} structure of $[\text{Ni}\{(\text{OPPh}_2)(\text{OPPh}_2)\text{N}\}_2(\text{DMF})_2]$ will be used as a reference for the lower-symmetry coordination environments of complexes 1–4. Initially, a complete geometry optimization of the structures of 1–4 at the BP86/TZVP/TZVPP level was performed. The optimized and crystallographic structures of 1–4 are in very good agreement. Thus, for the Ni–O, Ni–S, and Ni–Se bond lengths, the variations between theoretical and experimental bond lengths and angles are smaller than 0.03 Å and 2° , respectively (Table S2 in the SI).

Electronic Structure. The symmetry of complexes 1–4 is lower than O_h , as a result of significantly differing Ni–O_{eq} and Ni–E bond lengths (vide supra). As a consequence of this lower than O_h symmetry, complexes 1–4 exhibit very rhombic

EPR spectra (Table 1). Complex 5, on the other hand, exhibits D_{2h} symmetry, that is, an axially elongated O_h geometry along the O(DMF)–Ni–O(DMF) C_2 symmetry axis, with the chelating (O, O) ligands occupying the equatorial plane.⁵⁶ As can be seen in Figure 5, the D_{2h} model H^5 exhibits a ${}^3A_{2g}$

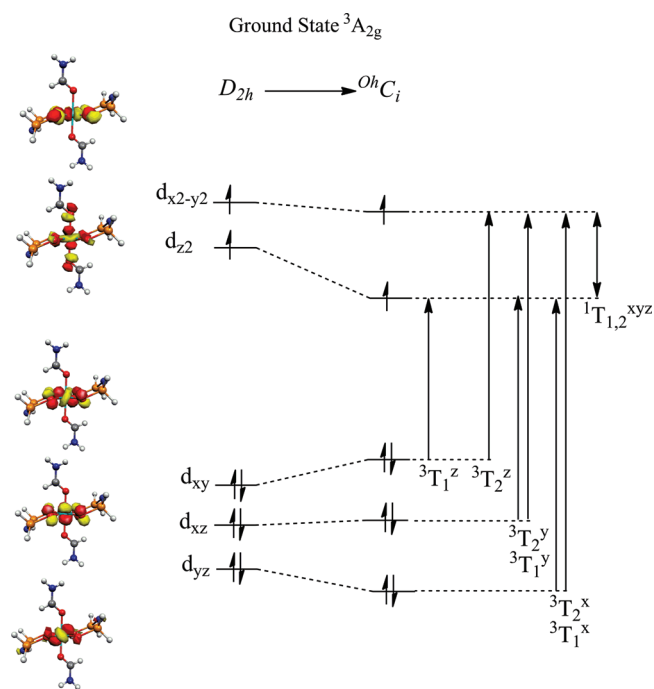


Figure 5. Metal d-based MOs and term symbols arising from single excitations for H^5 . The indicated orbital occupation pattern refers to the ${}^3A_{2g}$ ground state.

ground state, with a $d_{yz}^2 d_{xz}^2 d_{xy}^2 d_z^2 d_x^2 d_y^1$ electronic configuration. In the D_{2h} point group, the three components of the angular momentum operator transform as $L_x, B_{3g}; L_y, B_{2g};$ and L_z, B_{1g} . Both T_{1g} and T_{2g} states (in O_h symmetry) map onto ${}^1, {}^3T_{1,2}^z, {}^1, {}^3B_{1g}; T_{1,2}^y, B_{2g};$ and $T_{1,2}^x, B_{3g}$ states under D_{2h} symmetry and, hence, they can both spin–orbit couple with the ground state ${}^3A_{2g}$. The important single-electron excitations are those arising from the doubly occupied t_{2g} orbitals to the singly occupied e_g orbitals, namely, ${}^3T_2^z(d_{xy} \rightarrow d_{x^2-y^2})$, ${}^3T_1(d_{xy} \rightarrow d_z^2)$, ${}^3T_{1,2}^x(d_{yz} \rightarrow d_{x^2-y^2}, d_{yz} \rightarrow d_z^2)$, and ${}^3T_{1,2}^y(d_{xz} \rightarrow d_{x^2-y^2}, d_{xz} \rightarrow d_z^2)$, respectively, which take place within the $t_{2g}^5 e_g^3$ d shell, as well as the intra-SOMO ${}^1T_{1,2}^z(d_{x^2-y^2} \leftrightarrow d_z^2)$ transitions arising from both the $t_{2g}^5 e_g^3$ and $t_{2g}^6 e_g^4$ d shells (Scheme S1 in the SI).

Calculation of the zfs. In an effort to justify and interpret the trend in the experimental zfs values obtained for complexes 1–4 (Table 1), DFT and ab initio multiconfigurational studies were carried out on the H^1 – H^4 models, as described in the Materials and Methods section.

DFT Calculations. The results of the DFT calculations (presented in the SI) proved to be, at best, only in qualitative agreement with the experimental data. In fact, DFT approaches have been quite controversial in their ability to predict the magnetic properties of transition-metal compounds. Although they have been reasonably successful for Mn^{II} ^{85–87} and Mn^{III} ^{69,88} compounds, they have failed remarkably for T_d Co^{II} ⁸⁹ and O_h V^{III} ⁷² complexes. There are, also, cases, such as the $[\text{Cr}(\text{H}_2\text{O})_6]^{2+}$ complex,⁹⁰ in which DFT approaches led to correct results but for incorrect reasons. In fact, a certain degree of error cancellation has been frequently encountered in

Table 2. Computed zfs (cm^{-1}) Values and SOC Contributions to D , Derived by SA-CASSCF, NEVPT2, DDCI2, and SORCI Methods

model	state	SA-CASSCF		NEVPT2		DDCI2		SORCI		
		energy	D	energy	D	energy	D	energy	D	
H_1	${}^3B_1(z)$	5317	-61.7	7248	-53.111	6837	-5	7948	-47.5	
	${}^3B_2(y)$	5691	37.8	7828	26.2	7493	23	8529	21.4	
	${}^3B_3(x)$	6679	36.1	8388	20.5	7814	25	9305	19.4	
	${}^1B_1(z)$	22936	14.1	22758	14.6	23596	14	24480	15.1	
	${}^1B_2(y)$	23283	-7.5	23347	-7.3	24197	-7	25060	-6.3	
	${}^1B_3(x)$	24183	-6.5	23883	-6.7	24447	-6	25325	-7.1	
	$D^{\text{exp}} = 4.37$									
	second-order PT	$D_{2\text{nd PT}}^{\text{SOC}}$		-12.3		-5.8		-5.6		-5.0
	QDPT	$ D_{\text{exact}}^{\text{SOC}} $		5.2		3.1		4.2		3.1
		$E/D_{2\text{nd PT}}^{\text{SOC}}$		0.32		0.29		0.25		0.26
Ni spin population			1.92		1.92		1.83		1.92	
H_2	${}^3B_1(z)$	5042	-61.5	7093	-53.6	6498	-35.6	7564	-45.9	
	${}^3B_2(y)$	5345	38.6	7568	27.4	7168	27.5	8183	17.6	
	${}^3B_3(x)$	6769	38.6	8495	20.2	7588	17.0	9313	21.3	
	${}^1B_1(z)$	22644	14.3	22598	14.2	23114	6.8	24076	14.3	
	${}^1B_2(y)$	22916	-7.3	23081	-7.3	23704	-5.7	24713	-5.4	
	${}^1B_3(x)$	24220	-7.3	23994	-6.6	24329	-2.6	25092	-7.7	
	$D^{\text{exp}} = 3.41$									
	second-order PT	$D_{2\text{nd PT}}^{\text{SOC}}$		15.4		-5.7		7.4		-5.8
	QDPT	$ D_{\text{exact}}^{\text{SOC}} $		5.5		2.6		4.5		2.5
		$E/D_{2\text{nd PT}}^{\text{SOC}}$		0.21		0.18		0.26		0.27
Ni spin population			1.89		1.89		1.87		1.82	
H_3	${}^3B_3(x)$	5056	30.0	6752	32.4	6180	25.1	7315	21.3	
	${}^3B_2(y)$	5825	32.0	7242	28.7	6937	24.8	8103	20.5	
	${}^3B_1(z)$	6281	-82.0	8687	-46.8	7804	-62.1	9432	-52.1	
	${}^1B_3(x)$	22507	-6.5	22015	-8.1	22626	-7.5	22867	-7.3	
	${}^1B_2(y)$	23368	-6.9	22706	-7.5	23086	-7.2	23338	-6.8	
	${}^1B_1(z)$	23833	14.3	23930	13.8	24449	16.7	25577	15.8	
	$D^{\text{exp}} = 7.11$									
	second-order PT	$D_{2\text{nd PT}}^{\text{SOC}}$		-19.1		12.5		-10.8		-8.6
	QDPT	$ D_{\text{exact}}^{\text{SOC}} $		7.5		9.2		7.1		6.1
		$E/D_{2\text{nd PT}}^{\text{SOC}}$		0.14		0.16		0.18		0.19
Ni spin population			1.90		1.90		1.85		1.81	
H_4	${}^3B_3(x)$	5050	32.8	6965	19.4	6392	23.8	7915	23.1	
	${}^3B_2(y)$	5864	29.6	7751	23.5	7108	23.1	8901	20.7	
	${}^3B_1(z)$	6243	-79.9	8277	-54.4	7472	-45.1	9575	-38.1	
	${}^1B_3(x)$	22634	-6.9	22328	-6.9	22860	-6.6	24071	-7.2	
	${}^1B_2(y)$	23402	-6.8	23260	-5.9	23168	-4.8	25142	-5.5	
	${}^1B_1(z)$	23654	14.7	23747	14.0	24288	13.1	24272	11.7	
	$D^{\text{exp}} = 6.38$									
	second-order PT	$D_{2\text{nd PT}}^{\text{SOC}}$		-16.5		-10.3		3.5		4.7
	QDPT	$ D_{\text{exact}}^{\text{SOC}} $		6.6		6.4		5.5		4.5
		$E/D_{2\text{nd PT}}^{\text{SOC}}$		0.19		0.18		0.20		0.21
Ni spin population			1.91		1.91		1.86		1.81	

the calculation of zfs , in which the SOC contributions to the zfs are underestimated, whereas the SSC contributions are overestimated. While the formalism to calculate the zfs in a DFT framework is still under debate,⁶¹ no systematically accurate DFT method has so far been found. The data in the SI show that this situation is not changed by the latest proposals.⁶¹ In our experience, even relatively simple multiconfigurational ab initio calculations are preferable to any of the existing DFT methods. This is also the case for the present study, as will be summarized below.

Ab Initio Calculations. In general, for systems featuring near-orbital degeneracy, multiconfigurational ab initio calculations are more suitable than DFT methods because in these approaches all magnetic sublevels can be explicitly represented and treated on an equal footing.⁹¹ Such a treatment, in combination with QDPT, provides a suitable method to deal with problems of the kind met here. In the QDPT approach,

the SOC (and SSC) effects are treated through diagonalization of the BO SOC (and SSC) operators, on the basis of triplet and singlet roots of the BO Hamiltonian (extended to treat all $M = S, S - 1, \dots, -S$ components of a given state Ψ_i^{SM}), which is obtained from the SA-CASSCF(12,7), NEVPT2(12,7), MRDDCI(12,7), or SORCI(12,7) calculations (Table 2). Through diagonalization, the coupling of singlet and triplet states is treated to infinite order in the SOC. In addition to the zfs parameters D and E obtained from the PT eqs 6–8, real eigenvalues and complex eigenvectors of the (SOC + SSC)-extended Hamiltonian are obtained. The zfs parameters can be directly estimated by a matching procedure of the QDPT-calculated eigenvalues with those of the exact solution of the $S = 1$ SH problem for the zfs .⁴¹ A more complete approach is based on the effective Hamiltonian theory. This approach yields the entire D tensor rather than only the D and E values and has

Table 3. Individual SOC Contributions to D , as Derived from the NEVPT2/QDPT Method by Diagonalizing the Ground State with Each of the Involved Individual Excited States and Utilizing the Effective Hamiltonian Procedure for Determining the Value and Sign of D per State

effective Hamiltonian		model complexes			
		Me ₁	Me ₂	Me ₃	Me ₄
full QDPT 2 × 2 diagonalization	$D_{H_{\text{QDPT}}}^{\text{SOC}}$	-3.2	-2.8	11.1	-7.8
	${}^3\text{B}_1^z$	-57.1	${}^3\text{B}_1^z$ -57.4	${}^3\text{B}_3^x$ 32.7	${}^3\text{B}_3^x$ 41.9
	${}^3\text{B}_2^y$	22.7	${}^3\text{B}_2^y$ 34.1	${}^3\text{B}_2^y$ 23.5	${}^3\text{B}_2^y$ 33.8
	${}^3\text{B}_3^x$	30.5	${}^3\text{B}_3^x$ 15.9	${}^3\text{B}_1^z$ -39.9	${}^3\text{B}_1^z$ -83.3
	${}^1\text{B}_1^z$	15.3	${}^1\text{B}_1^z$ 15.7	${}^1\text{B}_3^x$ -8.1	${}^1\text{B}_3^x$ -7.7
	${}^1\text{B}_2^y$	-6.1	${}^1\text{B}_2^y$ -8.4	${}^1\text{B}_1^y$ 10.9	${}^1\text{B}_2^y$ -4.3
	${}^1\text{B}_3^x$	-8.7	${}^1\text{B}_3^x$ -2.3	${}^1\text{B}_2^z$ -7.3	${}^1\text{B}_1^z$ 12.1
sum	$D_{H_{\text{SOC}}}^{\text{SOC}}$	-3.3	-2.9	11.9	-7.5

recently been successfully applied to mono- and bimetallic complexes by Maurice et al.^{92,93}

SA-CASSCF. The most straightforward approach that complies with the ab initio strategy outlined above is the SA-CASSCF method. While being computationally efficient and conceptually satisfactory, it cannot be expected to be highly accurate. A state averaging procedure necessarily involves a compromise, and hence the description of each individual state is suffering as the number of states increases. More importantly, however, the nondynamic correlation recovered in these calculations is only a small part of the total correlation energy. The dynamic correlation has profound effects on the magnetic properties of a transition-metal complex because it strongly modifies the ionic character of the metal–ligand bonds by providing stronger covalent contributions. Hence, it significantly affects the transition energies between states of different character.^{94,95} Nevertheless, a well-defined strategy is to determine the number of relevant states from ligand-field considerations. This approach usually delivers a good reference wave function and, in our experience, has already led to satisfactory predictions of the zfs parameters.^{85,88,90} The underlying reason must be that the d–d multiplets are usually well described in the SA-CASSCF approach.⁹¹ However, the SA-CASSCF results can certainly be improved by including dynamic correlation, as will be shown below.

Excited-State Contribution to the zfs. To account for the importance of the excited-state contribution to the magnitude of the zfs, we have initially calculated the D value via the SA-CASSCF second-order PT, as well as the QDPT matching approach for all possible combinations of the 10 triplet and 15 singlet states of ${}^1\text{H}_1\text{--}{}^4\text{H}_4$. As described above, the sign and magnitude of D is estimated by the PT approach (eqs 6–8) $D_{2\text{nd PT}}^{\text{SOC}}$ and by matching the energy differences between the analytical eigenvalues of the $S = 1$ SH problem with those obtained from the QDPT approach $D_{\text{exact}}^{\text{SOC}}$. QDPT evidently performs better than PT, which makes sense because PT is an approximation to QDPT. Alternatively, D may be estimated by utilizing the effective Hamiltonian approach ($D_{H_{\text{QDPT}}}^{\text{SOC}}$)⁹² in which the zfs Hamiltonian (2) is directly compared with the effective Hamiltonian $\hat{H}^{\text{eff}} = \sum_i |\hat{\Psi}_i^{\text{SM}}\rangle E_i \langle \hat{\Psi}_i^{\text{SM}}|$, where $|\hat{\Psi}_i^{\text{SM}}\rangle$ are orthonormalized projections of the $|\Psi_i^{\text{SM}}\rangle$ states into the spanned space S_0 and E_i their ab initio energies. The calculated zfs values by both approaches are presented in Tables 2 and 3. Individual state contributions are readily identified and discussed in terms of both second-order PT and QDPT in the framework of the effective Hamiltonian matching procedure. For approximately decomposing the QDPT D

tensor into contributions from individual excited states, a series of diagonalizations is carried out that involve the ground-state magnetic sublevels and the magnetic sublevels of only one excited state at the time. This means that the SOC of the individual excited states with the ground state are treated nonperturbatively, while interference contributions that arise at third and higher order are neglected ($D_{H_{\text{SOC}}}^{\text{SOC}}$). As is seen in Table 3, the derived zfs values from the individual 2 × 2 diagonalizations compare reasonably well with those obtained utilizing the matching procedures with the full QDPT. In the present case, the SA-CASSCF PT methods overestimate the value of $|D|$ by a factor of 2. Nevertheless, there are cases in which PT performs equally well as QDPT.⁹⁰ It should be noted that the states are grouped according to their corresponding symmetry in idealized O_h symmetry. Hence, at increasing energies, the states are grouped as in Scheme S1 in the SI. The SOC component of the zfs parameter is mainly determined by the spin-conserving ${}^3\text{A}_{2g} \rightarrow {}^3\text{T}_{2g}$ transitions from the $t_{2g}^5 e_g^3$ configurations: ${}^3\text{A}_{2g} \rightarrow {}^3\text{B}_{1g}^z (d_{xy} \rightarrow d_{x^2-y^2})$, ${}^3\text{A}_{2g} \rightarrow {}^3\text{B}_{2g}^x (d_{yz} \rightarrow d_{x^2-y^2}, d_{yz} \rightarrow d_z^2)$, and ${}^3\text{A}_{2g} \rightarrow {}^3\text{B}_{3g}^y (d_{xz} \rightarrow d_{x^2-y^2}, d_{xz} \rightarrow d_z^2)$ in D_{2h} symmetry. In addition, the corresponding ${}^3\text{A}_{2g} \rightarrow {}^1\text{T}_{2g}$ spin-flipping transitions from both the $t_{2g}^5 e_g^3$ and $t_{2g}^4 e_g^4$ configurations also contribute to the zfs (Scheme S1 in the SI). However, the contribution from the $t_{2g}^4 e_g^4$ configuration is small ($<0.1 \text{ cm}^{-1}$). As follows from group theory and confirmed in the numerical calculations, the corresponding ${}^3\text{A}_{2g} \rightarrow {}^3\text{T}_{1g}$ derived transitions do not contribute at all. Hence, for all intents and purposes, the spectroscopic symmetry of the systems behaves as D_{2h} . Therefore, there are mainly two chemically important excited-state sets for calculation of the D^{SOC} component, a first comprising a combination of 4 and 11 triplet and singlet roots, respectively, denoted as the (4, 11) set, and a second with $t_{2g}^4 e_g^4$ excluded, denoted as the (4, 5) set.

In the cases of 1 and 2, by treating only the lowest ${}^3\text{A}_{1g} \rightarrow {}^1\text{T}_{2g}$ spin-flipping transitions in the (4, 5) set, equally satisfactory results are obtained, with a positive shift of only $\sim 0.2 \text{ cm}^{-1}$ with respect to the corresponding (4, 11) set. By contrast, for 3 and 4, better results are obtained with the (4, 5) set compared with the (4, 11) set. It should be noted, however, that in the case of 3, the best results are obtained with the (4, 8) set, which involves additional states that do not directly spin–orbit couple to the ground state. Evidently, all effects involving such states are higher than second order. Furthermore, from preliminary CAS-CI (12,7) calculations, the SSC contributions were found to be negligible ($\sim 0.02 \text{ cm}^{-1}$) and, therefore, the zfs in this class of Ni^{II} complexes is largely dominated by SOC interactions.

NEVPT2 Calculations. The calculated zfs data obtained for 1–4 by employing the NEVPT2/QDPT scheme are presented in Tables 2 and 3. The results are in satisfactory agreement with the experimental data for 1, 2, and 4. In the case of 3, the implemented NEVPT2 method appears to recover the major part of the differential dynamic correlation, and a significant improvement is achieved compared with the SA-CASSCF calculations. As can be seen in Table 2, the inclusion of dynamic correlation in the NEVPT2 scheme increases the energies of the ${}^3A_{2g} \rightarrow {}^3T_{2g}$ transitions and, consequently, decreases the absolute value of D , thus achieving zfs values that are significantly closer to the experimental ones than those delivered by SA-CASSCF. Similar observations have been recently made for a binuclear O_h Ni^{II} – Y^{III} complex.¹⁶

MRDDCI2 and SORCI Calculations. An alternative way to recover the dynamic correlation that is missing from the SA-CASSCF treatment is provided by the variational MRDDCI2 and SORCI methods. It has been shown that these methods are successful in calculating the magnetic properties of numerous metal complexes, namely, V^{III} ,⁷² $Cr^{II/III}$,⁹⁰ Mn^{II} ,⁸⁵ Mn^{III} ,⁶⁹ Fe^{IV} ,^{96,97} Co^{II} ,^{89,98} and Ni^{II} .⁷⁹ However, these methods are more restricted in their applicability because of the high computational effort. In particular, the SORCI method is expected to be the most accurate, but at the same time, it is also the most time-consuming. The reason is the additional variational step needed to build a more flexible wave function, which would also be more accurate with respect to the ones derived by pure perturbational treatments.⁶⁸ In an effort to compare the performance of the NEVPT2 method relative to the variational approaches, MRDDCI2 and SORCI calculations were performed on the same truncated models, H_1 – H_4 , and at the same level of calculation as that discussed in the Computational Details section. The results obtained by this treatment are shown in Table 2. The dynamic correlation treated by the variational methods increases the excitation energies further relative to the NEVPT2 results. Both effects work together to lower the calculated D values and thereby lead to excellent agreement with the experiment. However, as was already mentioned, a major drawback of these methodologies is the computational cost, which is significantly larger than the cost of NEVPT2, which typically takes less time than the preceding SA-CASSCF calculation. We can, therefore, conclude that, at a slight expense of accuracy, the NEVPT2 scheme provides the most efficient means to calculate the zfs for 1–4, even in the presence of soft ligands containing S and Se.

Magnetic Anisotropy and the Sign of D . Complexes 1–4 exhibit significant deviations from ideal O_h geometry, which are imposed (i) along the z axis by the coordination of different solvents and (ii) along the x/y equatorial axes by the different Ni^{II} -coordinated E atoms ($E = S, Se$). Along the z axis, the Ni–O(solvent) bond lengths range between 2.07 and 2.14 Å, whereas along the x/y axes, the Ni–E distances range between ~2.5 and 2.7 Å. A significant anisotropy is also observed in the experimental and calculated rhombicity E/D parameter of 1–4 (Tables 1 and 2).

In an effort to correlate the above observations with the anisotropic coordination environment around the Ni^{II} center, we have constructed a two-dimensional zfs map, in the NEVPT2 level, along the Ni–O(DMF) and Ni–E ($E = S, Se$) bond distances, based on the model structures H_1 and H_2 (Figure 6). By scanning these two bond distances, the effects of coordination by different solvents that exert different ligand-field strengths are expected to be probed. The Ni–O bond

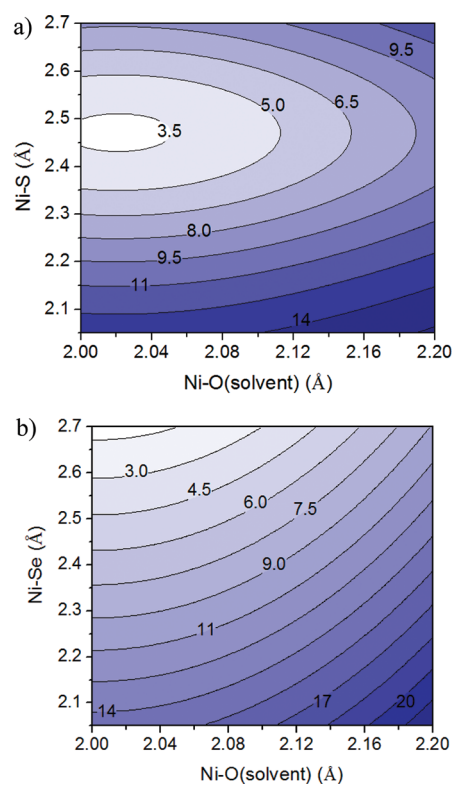


Figure 6. NEVPT2 (12,7) QDPT-calculated D values as a function of the Ni–O(DMF) and Ni–E ($E = S, Se$) bond distances for (a) H_1 and (b) H_2 .

distances are varied between 2.00 and 2.20 Å along the z axis, whereas the Ni–S and Ni–Se bond distances are varied between 2.05 and 2.70 Å along the x/y axes. It should be stressed that negligible effects on D were observed by Se over S coordination (Table 1). This is in contrast to the significant effects reported upon coordination of heavier halides to either $Ni^{II,21}$ or $Cr^{II/III}$ ⁹⁹ complexes. In Figure 6, the calculated D values by the QDPT-matching procedure based on the energy differences of the involved states are plotted along the δ_{Ni-O}^z and $\delta_{Ni-S/Se}^{x/y}$ bond distances. In agreement with the experiment, at the equilibrium distances on the xy plane ($\delta_{Ni-S}^{x/y} = 2.50$ Å and $\delta_{Ni-Se}^{x/y} = 2.65$ Å), the zfs values resemble those observed in H_1 , H_2 , H_3 , and H_4 for $\delta_{Ni-O(DMF)}^z = 2.08$ Å and $\delta_{Ni-O(THF)}^z = 2.12$ Å, respectively (Figure 6a,b). Furthermore, the scan along the interconversion pathway $D_{2h} \rightarrow {}^0A_1$ by varying the $\delta_{Ni-O(DMF)}^z$ distance, while keeping the equatorial Ni–S distance constant to the values for H_1 and H_2 ($\delta_{Ni-S/Se}^{x/y} = 2.5/2.65$ Å), reveals that the major SOC contribution to the zfs is dominated by the ${}^3A_{2g} \rightarrow {}^3B_{1g}^z(d_{xy} \rightarrow d_{x^2-y^2})$ single-electron excitations (Figure 7a,b). On the other hand, with the Ni–O(DMF) distance kept constant to the values of the equilibrium geometry of H_1 and H_2 , the scan along the interconversion pathway $D_{2h} \rightarrow {}^0A_1$ by varying the Ni–S/Se distances at $\delta_{Ni-S/Se}^{x/y} < 2.4/2.6$ Å shows that the SOC contribution to the zfs is also dominated by the ${}^3A_{2g} \rightarrow {}^3B_{1g}^z(d_{xy} \rightarrow d_{x^2-y^2})$ transition, whereas at $\delta_{Ni-S/Se}^{x/y} > 2.4/2.6$ Å, the order of the ${}^3T_{2g}$ and ${}^3T_{2g}$ states reverses; thus, SOC is dominated by the ${}^3A_{2g} \rightarrow {}^3B_{2g}^x(d_{yz} \rightarrow d_{x^2-y^2}, d_{yz} \rightarrow d_z^2)$ and ${}^3A_{2g} \rightarrow {}^3B_{3g}^z(d_{xz} \rightarrow d_{x^2-y^2}, d_{xz} \rightarrow d_z^2)$ transitions (Figure 7c,d). As seen in Figure 7c, at the equilibrium distance $\delta_{Ni-S}^{x/y} = 2.50$ Å, ${}^3B_{3g}^y$ + ${}^3B_{2g}^x$ and ${}^3B_{1g}^z$ are approximately degenerate; thus, the SOC contributions from these states to the zfs values cancel each other (Tables 2 and 3), and so an almost linear increase of D

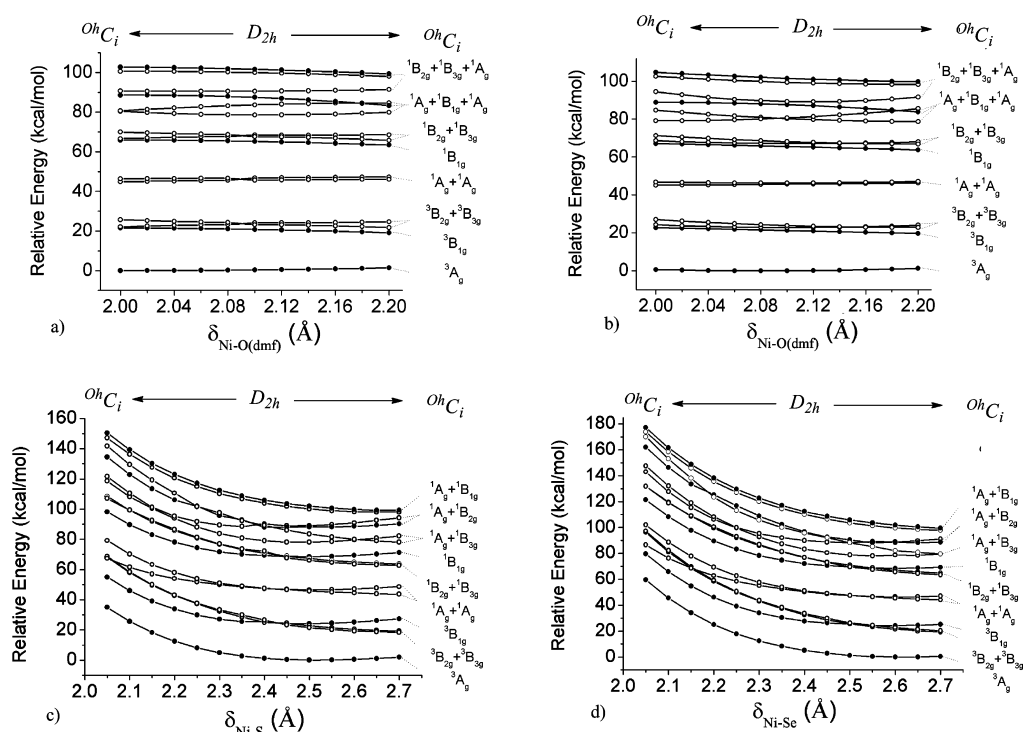


Figure 7. NEVPT2(12,7) scan along the $D_{2h} \rightarrow O_h C_i$ interconversion pathway for H^1 and H^2 . The ground, ${}^3A_{1g}$, and lowest excited SOC states, ${}^{3,1}T_{2g}$, are plotted along the pathway as a function of (a and b) the axial Ni–O(DMF) bond distances for H^1 and H^2 and (c and d) the equatorial Ni–S and Ni–Se bond distances, while keeping the axial Ni–O and Ni–O(DMF) bond distances constant to the values for H^1 and H^2 , respectively.

along the Ni–O(sol) bond is observed (Figure 6a). On the other hand, in the case of H^2 , at the equilibrium distance $\delta_{Ni-Se}^{x/y} > 2.65$ Å, the zfs is mainly dominated by the ${}^3A_{2g} \rightarrow {}^3B_{1g}(d_{xy} \rightarrow d_{x^2-y^2})$ single-electron excitation along the Ni–Se bond. It can, therefore, be concluded that the magnitude of D is sensitive to both the Ni–O(sol) and Ni–Se bond lengths (Figure 6b). In a more general perspective, if the zfs tensor was axial ($E \sim 0$), the large anisotropy along the z axis and xy plane would impose some competition for the sign of D at $\delta_{Ni-S/Se}^{x/y} > 2.4/2.6$ Å. However, a significant rhombicity has been observed experimentally and confirmed theoretically ($E/D > 0.2$), which renders the determination of the sign of D to be ambiguous. In any case, it is postulated that elongation along the z axis, as imposed by coordination of THF in the place of DMF, would result in less rhombic zfs tensors ($E/D \sim 0.2$), as indeed has been experimentally observed for H^3 and H^4 (Table 1). In systems with such large E/D values, second-order PT cannot determine the sign of D correctly.⁸⁶ However, in the QDPT approach, the magnetic sublevels are not strongly mixed; thus, for H^3 , the calculated ground magnetic sublevel is dominated by 65% of the ${}^3A_{2g}|0\rangle$ and 35% of the ${}^3A_{2g}|\pm 1\rangle$, whereas for H^4 , the corresponding values are 55% ${}^3A_{2g}|0\rangle$ and 45% ${}^3A_{2g}|\pm 1\rangle$. In the latter, the sign of D would be better described as positive, in accordance with the experimental findings (vide supra). This is readily observed in the case of 3 in the QDPT-matching procedure based on the effective Hamiltonian approach (Tables 2 and 3). In the case of 4, although the state order indicates a positive sign (Table 3 and Figure 7), the contribution from the ${}^3A_{2g} \rightarrow {}^3B_{1g}(d_{xy} \rightarrow d_{x^2-y^2})$ state is still highly negative (Table 3), resulting in an overall negative value. It should be stressed that, for an $O_h d^8$ system, LF theory,¹⁰⁰ as well as magnetometry arguments,^{14,15,101} concerning the sign of D postulates that respective elongation along the z axis (x/y axes) leads to negative (positive) D values.

Moreover, on the basis of the established effects of heavier metal-coordinated halides (vide supra), the magnitude of D for the Se-containing complexes (2 and 4) would be expected to be greater than the respective S-containing ones (1 and 3), which was not confirmed by our experiments. This points to the complex and, consequently, often counterintuitive nature of zfs as an electronic structure parameter. Our analysis shows that indeed expected postulates like those above are not linearly applicable in the systems investigated herein. In fact, as revealed by both experimental data and correlated ab initio multi-reference calculations, the magnitude and sign of D for complexes 1–4 are structure-dependent properties, strongly correlated with the anisotropic coordination environment around the Ni^{II} center.

CONCLUSIONS

In this work, a series of pseudooctahedral Ni^{II} complexes, namely, $trans-[Ni\{(OPPh_2)(EPh_2)N\}_2(sol)_2]$ ($E = S, Se$; sol = DMF, THF), have been synthesized and structurally characterized. The zfs parameters of these $S = 1$ systems have been estimated by magnetometry and accurately determined by HFEPR. The latter method provides the only option for such integer spin systems, which are often difficult to study by EPR spectroscopy at conventional fields and frequencies.¹² Following our previously established methodology, we have applied a multifrequency EPR approach,⁴³ in order to unequivocally assign the observed EPR signals for complexes 1–4, which afforded accurate zfs parameters. All 1–4 complexes exhibit rhombic zfs, with the magnitude of $|D|$ being ca. $3.5\text{--}4.0\text{ cm}^{-1}$ for 1 and 2 and $6.0\text{--}7.0\text{ cm}^{-1}$ for 3 and 4. In addition, significant magnetic anisotropy around the metal center is revealed by the rhombic parameter $|E/D|$, which ranges between 0.16 and 0.33 (Table 1), as well as by the g values

(mainly in the case of 4). The SH parameters (g and D) were also extracted by magnetic susceptibility data, in rather good agreement with those determined by HFEPR. It should be stressed, however, that this analysis cannot probe the rhombicity of the systems because it is not possible to include the rhombic E zfs component in the employed fitting procedures.

In addition to the experimental investigations, advanced computational methods were applied, in an effort to elucidate the origin of the zfs parameters and to translate them into electronic structure elements. Several DFT methodologies, including the most recently modified ones,⁶¹ have been applied, but none of them performs satisfactorily. On the other hand, good predictions of $|D|$ are provided by the ab initio SA-CASSCF method, upon treatment of the chemically important to SOC excited states. Improved results are obtained when dynamic correlation effects are included in the framework of the perturbative NEVPT2 second-order many-body PT, as well as the variational MRDDCI2 and SORCI methods. Dynamic correlation in all three methods tends to decrease the magnitude of zfs, thus leading to a better agreement with the experiment. For the investigated systems, second-order PT for the SOC is not adequate to accurately calculate the zfs. Thus, the best choice is provided by the QDPT-matching procedure based on the energy differences between the calculated magnetic sublevels, as well as by the effective Hamiltonian approach described by Maurice et al.^{92,93} Upon the inclusion of dynamic correlation, the d–d excitation energies increase relative to the SA-CASSCF results. This renders the second-order PT results somewhat more accurate. However, the QDPT-matching procedure still provides the most accurate results. Overall, the NEVPT2/QDPT method provides the best agreement between experiment and theory. The MRDDCI2/QDPT and SORCI/QDPT methods perform similarly well but at a high computational cost. Hence, NEVPT2/QDPT is the method of choice for calculation of large zfs values in transition-metal complexes.

The observed EPR silence of T_d NiS_4 and NiO_2S_2 complexes even at the highest magnetic fields and frequencies currently available (unpublished work) is attributed to large zfs values ($>30 \text{ cm}^{-1}$) of such $S = 1$ systems, an interpretation supported by computational studies,^{35,79} or experimental findings in other T_d NiS_4 systems.^{30,31} On the other hand, in the O_h Ni^{II} complexes 1–4 investigated herein, the solvent coordination shifts the excited states in higher energies with respect to the ground state, thus reducing the strength of SOC and subsequently the magnitude of the zfs values ($3\text{--}7 \text{ cm}^{-1}$).

In both T_d and O_h Ni^{II} complexes of the above type, the SSC contributions were found to be negligible and, therefore, the zfs is largely dominated by SOC interactions, as is also the case for T_d Co^{II} complexes bearing either $[(\text{SPR}_2)(\text{SPR}'_2)\text{N}]^{-89}$ or other types of ligands.⁹⁸ On the other hand, the SSC contributions play a nonnegligible role, for instance, in $[\text{Cr}(\text{H}_2\text{O})_6]^{2+}$,⁹⁰ $[\text{Mn}(\text{acac})_3]^{3+}$,⁶⁹ and other Mn^{III} ⁸⁸ or V^{III} ⁷² complexes. In fact, only for very large zfs values ($>10 \text{ cm}^{-1}$), the SSC could be justifiably neglected. For the other cases, SSC may or may not have a significant impact on the magnitude of zfs.

Furthermore, the work presented herein probes, both experimentally and computationally, zfs effects of Se coordination to Ni^{II} . Calculations on the S-containing ^1H model show an almost linear increase of D as the Ni–O(sol) bond length increases (Figure 6a). On the other hand, for the Se-containing

^2H model, the magnitude of D is shown to be sensitive to both the Ni–O(sol) and Ni–Se bond lengths (Figure 6b). Analogous experimental and computational studies should be carried out on additional complexes containing Ni^{II} –Se bonds, in order to draw more general conclusions. Such investigations would provide extra insight into the biological properties of nickel, owing to the existence of Ni–Se bonds in the oxygen-tolerant Ni–Fe–Se hydrogenases.^{102,103}

■ ASSOCIATED CONTENT

📄 Supporting Information

X-ray crystallographic data in CIF format, synthesis and characterization of complexes 3 and 4, crystallographic data for complexes 3 and 4 (Table S1), calculated and crystallographic bond lengths and angles and relevant Löwdin bond orders for complexes 1–4 (Table S2), EPR spectra and corresponding simulations for complexes 1–3, respectively (Figures S1–S3), state correlation diagram of the model 5^{H} along the $O_h \rightarrow D_{2h}$ elongation pathway (Scheme S1), experimental and computed zfs values by DFT calculations for complexes 1–4 (Table S3), and relevant analysis. This material is available free of charge via the Internet at <http://pubs.acs.org>.

■ AUTHOR INFORMATION

Corresponding Author

*E-mail: krzystek@magnet.fsu.edu (J.K.), frank.neese@mpi-mail.mpg.de (F.N.), kyritsis@chem.uoa.gr (P.K.).

Notes

The authors declare no competing financial interest.

■ ACKNOWLEDGMENTS

We are grateful to the Special Account of the University of Athens (Grant 7575 to P.K.), the Max-Planck Society (to D.M. and F.N.), and the EPSRC, U.K. (to A.M.W. and N.R.) for financial support of this work. HFEPR studies (by J.K.) were supported by the NHMFL, which is funded by the NSF through Cooperative Agreement DMR 0654118, the State of Florida, and the DOE. We thank Dr. Andrew Ozarowski for his EPR simulation and fitting program *SPIN*. The reviewers of the manuscript are thanked for their constructive comments.

■ REFERENCES

- (1) Nickel and Its Surprising Impact in Nature: Metal Ions in Life Sciences, Sigel, A.; Sigel, H.; Sigel, R. K. O., Eds, John Wiley and Sons Ltd 2007.
- (2) Cotton, F. A.; Wilkinson, G.; Murillo, C. A.; Bochmann, M. *Advanced Inorganic Chemistry*, 6th Ed.; Wiley Interscience: New York, 1999, pp 838–846.
- (3) Ragsdale, S. W. *J. Biol. Chem.* **2009**, *284*, 18571–18575.
- (4) Halcrow, M. A.; Christou, G. *Chem. Rev.* **1994**, *94*, 2421–2481.
- (5) Gordon, J. C.; Kubas, G. J. *Organometallics* **2010**, *29*, 4682–4701.
- (6) Heinekey, D. M. *J. Organomet. Chem.* **2009**, *694*, 2671–2680.
- (7) Bouwman, E.; Reedijk, J. *Coord. Chem. Rev.* **2005**, *249*, 1555–1581.
- (8) Panda, R.; Zhang, Y. G.; McLauchlan, C. C.; Rao, P. V.; de Oliveira, F. A. T.; Munck, E.; Holm, R. H. *J. Am. Chem. Soc.* **2004**, *126*, 6448–6459.
- (9) Rao, P. V.; Bhaduri, S.; Jiang, J. F.; Hong, D.; Holm, R. H. *J. Am. Chem. Soc.* **2005**, *127*, 1933–1945.
- (10) Bridgeman, A. J. *Dalton Trans.* **2008**, 1989–1992.
- (11) Frommel, T.; Peters, W.; Wunderlich, H.; Kuchen, W. *Angew. Chem., Int. Ed.* **1993**, *32*, 907–909.

- (12) Krzystek, J.; Ozarowski, A.; Telsler, J. *Coord. Chem. Rev.* **2006**, *250*, 2308–2324.
- (13) Solomon, E. I. *Inorg. Chem.* **2005**, *44*, 723–726.
- (14) Boca, R. *Coord. Chem. Rev.* **2004**, *248*, 757–815.
- (15) Titis, J.; Boca, R. *Inorg. Chem.* **2010**, *49*, 3971–3973.
- (16) Maurice, R.; Vendier, L.; Costes, J.–P. *Inorg. Chem.* **2011**, *50*, 11075–11081.
- (17) van Dam, P. J.; Klaassen, A. A. K.; Reijerse, E. J.; Hagen, W. R. J. *Magn. Reson.* **1998**, *130*, 140–144.
- (18) Collison, D.; Helliwell, M.; Jones, V. M.; Mabbs, F. E.; McInnes, E. J. L.; Riedi, P. C.; Smith, G. M.; Pritchard, R. G.; Cross, W. I. J. *Chem. Soc., Faraday Trans.* **1998**, *94*, 3019–3025.
- (19) Pardi, L. A.; Hassan, A. K.; Hulsbergen, F. B.; Reedijk, J.; Spek, A. L.; Brunel, L. C. *Inorg. Chem.* **2000**, *39*, 159–164.
- (20) Mrozinski, J.; Skorupa, A.; Pochaba, A.; Dromzecz, Y.; Verdaguer, M.; Goovaerts, E.; Varcammen, H.; Korybut–Daszkiewicz, B. *J. Mol. Struct.* **2001**, *559*, 107–118.
- (21) Krzystek, J.; Park, J. H.; Meisel, M. W.; Hitchman, M. A.; Stratemeier, H.; Brunel, L. C.; Telsler, J. *Inorg. Chem.* **2002**, *41*, 4478–4487.
- (22) Yang, E. C.; Kirman, C.; Lawrence, J.; Zakharov, L. N.; Rheingold, A. L.; Hill, S.; Hendrickson, D. N. *Inorg. Chem.* **2005**, *44*, 3827–3836.
- (23) Rogez, G.; Rebillay, J. N.; Barra, A. L.; Sorace, L.; Blondin, G.; Kirchner, N.; Duran, M.; van Slageren, J.; Parsons, S.; Ricard, L.; Marvilliers, A.; Mallah, T. *Angew. Chem., Int. Ed.* **2005**, *44*, 1876–1879.
- (24) Dobrzynska, D.; Jerzykiewicz, L. B.; Duczmal, M.; Wojciechowska, A.; Jablonska, K.; Palus, J.; Ozarowski, A. *Inorg. Chem.* **2006**, *45*, 10479–10486.
- (25) Desrochers, P. J.; Telsler, J.; Zvyagin, S. A.; Ozarowski, A.; Krzystek, J.; Vivic, D. A. *Inorg. Chem.* **2006**, *45*, 8930–8941.
- (26) Charron, G.; Bellot, F.; Cisnetti, F.; Pelosi, G.; Rebillay, J. N.; Riviere, E.; Barra, A. L.; Mallah, T.; Policar, C. *Chem.—Eur. J.* **2007**, *13*, 2774–2782.
- (27) Rebillay, J. N.; Charron, G.; Riviere, E.; Guillot, R.; Barra, A. L.; Serrano, M. D.; van Slageren, J.; Mallah, T. *Chem.—Eur. J.* **2008**, *14*, 1169–1177.
- (28) Nieto, I.; Bontchev, R. P.; Ozarowski, A.; Smirnov, D.; Krzystek, J.; Telsler, J.; Smith, J. M. *Inorg. Chim. Acta* **2009**, *362*, 4449–4460.
- (29) (a) Wojciechowska, A.; Daszkiewicz, M.; Staszak, Z.; Trusz–Zdybek, A.; Bieńko, A.; Ozarowski, A. *Inorg. Chem.* **2011**, *50*, 11532–11542. (b) Desrochers, P. J.; Sutton, C. A.; Abrams, M. L.; Ye, S.; Neese, F.; Telsler, J.; Ozarowski, J.; Krzystek, J. *Inorg. Chem.* **2012**, *51*, 2793–2805.
- (30) Kowal, A. T.; Zambrano, I. C.; Moura, I.; Moura, J. J. G.; Legall, J.; Johnson, M. K. *Inorg. Chem.* **1988**, *27*, 1162–1166.
- (31) Vanelp, J.; Peng, G.; Searle, B. G.; Mitrakirtley, S.; Huang, Y. H.; Johnson, M. K.; Zhou, Z. H.; Adams, M. W. W.; Maroney, M. J.; Cramer, S. P. *J. Am. Chem. Soc.* **1994**, *116*, 1918–1923.
- (32) Vongtragool, S.; Gorshunov, B.; Dressel, M.; Krzystek, J.; Eichhorn, D. M.; Telsler, J. *Inorg. Chem.* **2003**, *42*, 1788–1790.
- (33) van Slageren, J.; Vongtragool, S.; Gorshunov, B.; Mukhin, A. A.; Karl, N.; Krzystek, J.; Telsler, J.; Muller, A.; Sangregorio, C.; Gatteschi, D.; Dressel, M. *Phys. Chem. Chem. Phys.* **2003**, *5*, 3837–3843.
- (34) Hagen, W. R. *Coord. Chem. Rev.* **1999**, *190–192*, 209–229.
- (35) Ferentinos, E.; Maganas, D.; Raptopoulou, C. P.; Terzis, A.; Psycharis, V.; Robertson, N.; Kyritsis, P. *Dalton Trans.* **2011**, *40*, 169–180.
- (36) Neese, F.; Ames, W.; Christian, G.; Kampa, M.; Liakos, D. G.; Pantazis, D. A.; Roemelt, M.; Surawatanawong, P.; Shengfa, Y. E. In *Adv. Inorg. Chem.*; Rudi van, E., Jeremy, H., Eds.; Academic Press: 2010; Vol. 62, p 301.
- (37) Neese, F. *Biol. Magn. Reson.* **2009**, *28*, 175–229.
- (38) Bain, G. A.; Berry, J. F. *J. Chem. Educ.* **2008**, *85*, 532–536.
- (39) Hassan, A. K.; Pardi, L. A.; Krzystek, J.; Sienkiewicz, A.; Goy, P.; Rohrer, M.; Brunel, L. C. *J. Magn. Reson.* **2000**, *142*, 300–312.
- (40) Abragam, A.; Bleaney, B., *Electron Paramagnetic Resonance of Transition Ions*; Dover Publications: New York, 1986.
- (41) Atherton, N. M. *Principles of Electron Spin Resonance*; Ellis Horwood PTR Prentice Hall ed., 1993.
- (42) Burkhardt, A.; Plass, W. *Inorg. Chem. Commun.* **2008**, *11*, 303–306.
- (43) Krzystek, J.; Zvyagin, S. A.; Ozarowski, A.; Trofimenko, S.; Telsler, J. *J. Magn. Reson.* **2006**, *178*, 174–183.
- (44) Baranowski, J.; Cukierda, T.; Jezowska–Trzebiatowska, B.; Kozłowski, H. *Chem. Phys. Lett.* **1976**, *39*, 606–608.
- (45) McWeeny, R. *Methods of Molecular Quantum Mechanics*; Academic: London, 1992.
- (46) Neese, F.; Solomon, E. I. *Inorg. Chem.* **1998**, *37*, 6568–6582.
- (47) Neese, F. *J. Chem. Phys.* **2005**, *122*, 34107.
- (48) Neese, F. *Wiley Interdisciplinary Reviews: Computational Molecular Science* **2011**, *2*, 73–78.
- (49) Becke, A. D. *Phys. Rev. A* **1988**, *38*, 3098–3100.
- (50) Becke, A. D. *J. Chem. Phys.* **1993**, *98*, 5648–5652.
- (51) Lee, C.; Yang, W.; Parr, R. G. *Phys. Rev. B* **1988**, *37*, 785–789.
- (52) Schäfer, A.; Huber, C.; Ahlrichs, R. *J. Chem. Phys.* **1994**, *100*, 5829–5836.
- (53) Hess, B. A. *Phys. Rev. A* **1985**, *32*, 756–763.
- (54) Hess, B. A. *Phys. Rev. A* **1986**, *333*, 3742–3748.
- (55) Jansen, G.; Hess, B. A. *Phys. Rev. A* **1989**, *39*, 6016–6017.
- (56) Cristurean, A.; Irisli, S.; Marginean, D.; Rat, C.; Silvestru, A. *Polyhedron* **2008**, *27*, 2143–2150.
- (57) Tao, J. M.; Perdew, J. P.; Staroverov, V. N.; Scuseria, G. E. *Phys. Rev. Lett.* **2003**, *91*, 146401–146404.
- (58) Staroverov, V. N.; Scuseria, G. E.; Tao, J.; Perdew, J. P. *J. Chem. Phys.* **2003**, *119*, 12129–12137.
- (59) Weigend, F.; Ahlrichs, R. *Phys. Chem. Chem. Phys.* **2005**, *7*, 3297–3305.
- (60) Neese, F. *J. Chem. Phys.* **2007**, *127*, 164112.
- (61) Schmitt, S.; Jost, P.; van Wüllen, C. *J. Chem. Phys.* **2011**, *134*, 194113.
- (62) Pederson, M. R.; Khanna, S. N. *Phys. Rev. B* **1999**, *60*, 9566–9572.
- (63) Ganyushin, D.; Neese, F. *J. Chem. Phys.* **2006**, *125*, 024103.
- (64) Ganyushin, D.; Neese, F. *J. Chem. Phys.* **2008**, *128*, 114117.
- (65) Angeli, C.; Borini, S.; Cestari, M.; Cimiraglia, R. *J. Chem. Phys.* **2004**, *121*, 4043–4049.
- (66) Angeli, C.; Cimiraglia, R.; Evangelisti, S.; Leininger, T.; Malrieu, J.–P. *J. Chem. Phys.* **2001**, *114*, 10252–10264.
- (67) Angeli, C.; Cimiraglia, R.; Malrieu, J.–P. *J. Chem. Phys.* **2002**, *117*, 9138–9153.
- (68) Neese, F. *J. Chem. Phys.* **2003**, *119*, 9428–9443.
- (69) Neese, F. *J. Am. Chem. Soc.* **2006**, *128*, 10213–10222.
- (70) Silvestru, A.; Bilc, D.; Rosler, R.; Drake, J. E.; Haiduc, I. *Inorg. Chim. Acta* **2000**, *305*, 106–110.
- (71) Boca, R. *Magnetic Functions Beyond the Spin–Hamiltonian*; Springer ed.; *Structure and Bonding*, 2006; Vol. 117.
- (72) Ye, S.; Neese, F.; Ozarowski, A.; Smirnov, D.; Krzystek, J.; Telsler, J.; Liao, J.–H.; Hung, C.–H.; Chu, W.–C.; Tsai, Y.–F.; Wang, R.–C.; Chen, K.–Y.; Hsu, H.–F. *Inorg. Chem.* **2010**, *49*, 977–988.
- (73) Carlin, R. L. *Magnetochemistry*; Springer Verlag, Berlin, 1986.
- (74) Figgis, B. N.; Hitchman, M. A. *Ligand Field Theory and Its Applications*; Wiley–VCH, 2000.
- (75) Orchard, A. F. *Magnetochemistry*; Oxford University Press, Oxford UK, 2003.
- (76) Bendix, J.; Brorson, M.; Schäfer, C. E. *Inorg. Chem.* **1993**, *32*, 2838–2849.
- (77) (a) Rosen, W.; Busch, D. H. *Inorg. Chem.* **1970**, *9*, 262–265. (b) Baho, N.; Zargarian, D. *Inorg. Chem.* **2007**, *46*, 299–308.
- (78) Wasserman, E.; Snyder, L. C.; Yager, W. A. *J. Chem. Phys.* **1964**, *41*, 1763–1772.
- (79) Maganas, D.; Grigoropoulos, A.; Staniland, S. S.; Chatziefthimiou, S. D.; Harrison, A.; Robertson, N.; Kyritsis, P.; Neese, F. *Inorg. Chem.* **2010**, *49*, 5079–5093.
- (80) Cupertino, D.; Keyte, R.; Slawin, A. M. Z.; Williams, D. J.; Woollins, J. D. *Inorg. Chem.* **1996**, *35*, 2695–2697.

- (81) Roesler, R.; Silvestru, C.; Georgina, Espinosa–Perez; Haiduc, I.; Cea–Olivares, R. *Inorg. Chim. Acta* **1996**, *241*, 47–54.
- (82) Bhattacharyya, P.; Novosad, J.; Phillips, J.; Slawin, A. M. Z.; Williams, D. J.; Woollins, J. D. J. *Chem. Soc., Dalton Trans.* **1995**, 1607–1613.
- (83) Churchil, M. R.; Cooke, J.; Fennesse, J. P.; Wormald, J. *Inorg. Chem.* **1971**, *10*, 1031–1035.
- (84) Simón–Manso, E.; Valderrama, M.; Boys, D. *Inorg. Chem.* **2001**, *40*, 3647–3649.
- (85) Zein, S.; Neese, F. J. *Phys. Chem. A* **2008**, *112*, 7976–7983.
- (86) Zein, S.; Duboc, C.; Lubitz, W.; Neese, F. *Inorg. Chem.* **2007**, *47*, 134–142.
- (87) Duboc, C.; Phoeung, T.; Zein, S.; Pécaut, J.; Collomb, M. N.; Neese, F. *Inorg. Chem.* **2007**, *46*, 4905–4916.
- (88) Duboc, C.; Ganyushin, D.; Sivalingam, K.; Collomb, M.–N.; Neese, F. J. *Phys. Chem. A* **2010**, *114*, 10750–10758.
- (89) Maganas, D.; Sottini, S.; Kyritsis, P.; Groenen, E. J. J.; Neese, F. *Inorg. Chem.* **2011**, *50*, 8741–8754.
- (90) Liakos, D. G.; Ganyushin, D.; Neese, F. *Inorg. Chem.* **2009**, *48*, 10572–10580.
- (91) Neese, F.; Petrenko, T.; Ganyushin, D.; Olbrich, G. *Coord. Chem. Rev.* **2007**, *251*, 288–327.
- (92) Maurice, R.; Bastardis, R.; de Graaf, C.; Suaud, N.; Mallah, T.; Guihéry, N. J. *Chem. Theor. Comput.* **2009**, *5*, 2977–2984.
- (93) Maurice, R.; Guihéry, N.; Bastardis, R.; de Graaf, C. J. *Chem. Theor. Comput.* **2010**, *6*, 55–65.
- (94) Zaitsevskii, A.; Malrieu, J.–P. *Int. J. Quantum Chem.* **1995**, *55*, 117–125.
- (95) Zaitsevskii, A.; Malrieu, J.–P. *Chem. Phys. Lett.* **1996**, *250*, 366–372.
- (96) Schöneboom, J. C.; Neese, F.; Thiel, W. J. *Am. Chem. Soc.* **2005**, *127*, 5840–5853.
- (97) Berry, J. F.; de Beer–George, S.; Neese, F. *Phys. Chem. Chem. Phys.* **2008**, *10*, 4361–4374.
- (98) Sundararajan, M.; Ganyushin, D.; Ye, S.; Neese, F. *Dalton Trans.* **2009**, 6021–6036.
- (99) Karunadasa, H. I.; Arquero, K. D.; Berben, L. A.; Long, J. R. *Inorg. Chem.* **2010**, *49*, 4738–4740.
- (100) Neese, F.; Solomon, E. I. *Magnetism – From Molecules to Materials*; Miller, J. S.; Drillon, M. ed., 2003; Vol. IV.
- (101) (a) Mabbs, F. E., Machin, D. J. *Magnetism and Transition Metal Complexes*; Dover Publications Inc.: New York, 2008, (b) Mabbs, F. E., Machin, D. J. *Magnetism and Transition Metal Complexes*; Chapman and Hall New York, 1973.
- (102) Garcin, E.; Vernede, X.; Hatchikian, E. C.; Volbeda, A.; Frey, M.; Fontecilla–Camps, J. C. *Struct. Fold. Des.* **1999**, *7*, 557–566.
- (103) Marques, M. C.; Coelho, R.; de Lacey, A. L.; Pereira, I. A. C.; Matias, P. M. J. *Mol. Biol.* **2010**, *396*, 893–907.